Experimental Investigations and Numerical Assessment of Liquid Velocity Profiles and Turbulence for Single- and Two-phase Flow in a Constricted Vertical Pipe

Tas-Köhler, S.; Neumann-Kipping, M.; Liao, Y.; Bieberle, A.; Hampel, U.;

Originally published:

August 2022

International Journal of Multiphase Flow 157(2022), 104224

DOI: https://doi.org/10.1016/j.ijmultiphaseflow.2022.104224

Perma-Link to Publication Repository of HZDR:

https://www.hzdr.de/publications/Publ-35307

Experimental Investigations and Numerical Assessment of Liquid Velocity Profiles and Turbulence for Single- and Two-phase Flow in a Constricted Vertical Pipe

Sibel Tas-Koehler[1*†], Martin Neumann-Kipping[2†], Yixiang Liao[1], André Bieberle[1], Uwe Hampel[1,2]

[1] Institute of Fluid Dynamics, Helmholtz-Zentrum Dresden-Rossendorf, Bautzner Landstraße 400, 01328 Dresden, Germany

[2] Chair of Imaging Techniques in Energy and Process Engineering, Technische Universität Dresden, 01062 Dresden, Germany

* Corresponding author (E-mail: s.tas@hzdr.de)

[†] These authors contributed equally to this work

Abstract

In this work, the capabilities of state-of-the-art turbulence models are compared for a three-dimensional flow field within a constricted vertical pipe. The considered flow domain is a vertical pipe section with a baffle-shaped flow constriction which leads to the development of a jet flow through and a recirculation flow region behind the constriction. Different Reynolds-Average Navier-Stokes (RANS) and Large Eddy Simulation (LES) models were tested for single- and two-phase flow simulations. In the two-phase simulations, bubble-induced turbulence (BIT) was also considered by adding source terms in the k and ε/ω equations. The results are validated against experimental data. We employed hot-film anemometry (HFA) for liquid velocity measurement and combined it with ultrafast X-ray computed tomography (UFXCT), which provides gas phase data. Based on the local phase-indicator function obtained from the tomographic image data, we can correct HFA signals, which become corrupted by bubble contacts. We found that for single-phase flow all RANS models predict axial velocity well while radial velocity prediction is inadequate. LES models, however, achieve a better prediction of the latter. For two-phase flow, the axial component of the liquid velocity is well captured by all RANS models and the radial component of the liquid velocity is predicted better than for single-phase flow. In general,

the computationally less costly RNG k-ε model performs similar to the SSG RSM model and can therefore be recommended for simulation of complex flow scenarios.

Keywords: bubbly two-phase flow, computed tomography, hot-film anemometry, liquid velocity, turbulent kinetic energy, CFD modelling

Nomenclature

Latin symbols

a, b, c	HFA calibration parameter [-]	$N_{i,j}$	Number of image pixels [-]
d_B	Bubble diameter [mm]	N_k	Number of images [-]
C_D	Drag coefficient [-]	p	Pressure [Pa]
C_L	Lift coefficient [-]	$\bar{p}$	Filtered pressure [Pa]
C_W	Wall lubrication coefficient [-]	R, r	Pipe radius [m]
C_{VM}	Virtual mass coefficient [-]	$\bar{S}_{ij}$	Filtered strain rate tensor [s^{-1}]
$d_\perp$	Maximum horizontal bubble dimension [mm]	**Greek symbols**	
$Eo_\perp$	Eötvös number depending on $d_\perp$ [-]	α	Volume fraction [-]
Eo	Eötvös number [-]	$\Delta z_{i,j}$	Image plane distance map [m]
F	Cross-correlation function [-]	Δk	Time shift [-]
f	Image frequency [-]	μ	Dynamic viscosity [$kg \cdot m^{-1} \cdot s^{-1}$]
F_D	Drag force per unit volume [$N \cdot m^{-3}$]	μ_t	SGS eddy viscosity [$kg \cdot m^{-1} \cdot s^{-1}$]
F_L	Lift force per unit volume [$N \cdot m^{-3}$]	$\mu_{i,j,k}$	X-ray attenuation coefficients [mm^{-1}]
F_W	Wall lubrication force per unit volume [$N \cdot m^{-3}$]	ξ	Phase indicator function
F_{Disp}	Turbulent dispersion force per unit volume [$N \cdot m^{-3}$]	τ	Bubble-induced time scale [s]
F_{VM}	Virtual mass force per unit volume [$N \cdot m^{-3}$]	τ_{ij}	SGS stress tensor [$kg \cdot m^{-1} \cdot s^{-2}$]
g	Gain value	${\tau_{ij}}^{Lam}, {\tau_{ij}}^{Turb}$	Stress tensor (laminar and turbulent) [$kg \cdot m^{-1} \cdot s^{-2}$]
j	Superficial velocity [$m \cdot s^{-1}$]	τ_f	Scanning time per image pair [s]
L, l	Test section length [mm]	τ_r	Characteristic time response [s]
M_i	Source term in i-th direction [$kg \cdot m^{-2} \cdot s^{-2}$]	τ_s	Sampling time [s]
k	Turbulent kinetic energy [$m^2 \cdot s^{-2}$], Yaw coefficient [-]	ρ	Density [$kg \cdot m^{-3}$]

S_K	Source term due to turbulent kinetic energy [N·m^{-2}·s^{-1}]	**Subscripts and Superscripts**	
S_ε	Source term due to turbulent dissipation rate [N·m^{-2}·s^{-2}]	bdg	Wheatstone bridge
S_ω	Source term due to turbulent frequency [N·m^{-4}]	bin	Binarized data set
u_i	Velocity in i-th direction [m·s^{-1}]	g	Gas phase
$\bar{u}_i$	Filtered velocity in i-th direction [m·s^{-1}]	i, j	Pixel (spatial) indices
$\bar{u}_{i,j}$	Velocity map (axial) from tomographic image data [m·s^{-1}]	k	Phase indicator, Image pair number
$\overline{u' u'}$, $\overline{v' v'}$	Turbulent fluctuation (axial and radial) [m^{-2}·s^{-2}]	l	Liquid phase
$\overline{u'u'}$	Shear stress [m^{-2}·s^{-2}]	low	Lower imaging plane
U	Voltage [V]	n	Normal component of velocity
$\dot{V}$	Volumetric flow rate [m^3·s^{-1}]	off	Offset
v	Radial velocity [m·s^{-1}]	out	Output
v_{noz}	Flow velocity at calibration nozzle [m·s^{-1}]	t	Tangential component of velocity
w	Pixel weights (inner pipe cross-section) [-]	tip	HFA probe tip position
x, y	Spatial coordinate [m]	tp	Two-phase flow
z	Axial position [m]	up	Upper imaging plane

Acronyms

BIT: Bubble-Induced Turbulence

CFD: Computational Fluid Dynamics

HFA: Hot-Film Anemometry

RANS: Reynolds-Averaged Navier-Stokes

RNG: Re-Normalization Group

LES: Large Eddy Simulation

SGS: Sub-grid Scale

SSG: Speziale-Sarkar-Gatski

SST: Shear Stress Transport

TKE: Turbulent Kinetic Energy

UFXCT: Ultrafast X-ray Computed Tomography

1 Introduction

The detailed understanding of turbulent two-phase bubbly flows is of great importance in many engineering applications, such as e.g. nuclear reactors, stirred tanks, airlift reactors and bubble columns. No matter, whether single or two-phase flow, turbulent flows can in principle be simulated by resolving all turbulent structures in space and time using direct numerical simulation (DNS) method. However, this method is still limited to rather low Reynolds numbers, as it requires extremely high computational effort. Thus, simulation of turbulent flows requires a reduction of the resolved length scales and time scales. By doing so, closure models are required to model the unresolved scales. For this reason, various turbulence models have been developed that can be used in computational fluid dynamics (CFD) simulations, each having its own advantages and limitations. The crucial point is the application of the appropriate turbulence model depending on the flow structure.

Different turbulence approaches such as Reynolds-Averaged Navier-Stokes (RANS) and large eddy simulation (LES) have been extensively studied in the literature for single-phase flows (Hossain *et al.* (2017); Lim *et al.* (2018); Loyseau *et al.* (2018)), but insufficiently for two-phase flows, as turbulence modelling in two-phase flows is more complex due to the motion of the gas bubbles and their interaction with the liquid phase. It is assumed that there are two different mechanisms of turbulence generation in a two-phase flow. The first mechanism is shear-induced turbulence (SIT), which is due to the momentum exchange resulting from conventional turbulence (i.e. random motions within the liquid phase). For SIT, the turbulence parameters are calculated by the applied turbulence model for single-phase flow. The second mechanism is bubble-induced turbulence (BIT), which takes into account turbulence generation due to the interfacial energy transfer between bubbles and liquid.

To reduce the complexity of the modelling, early studies on turbulence modelling of two-phase flows only considered the turbulence caused by the liquid phase, i.e. the SIT (Olmos *et al.* (2003); Padial *et al.* (2000); Pfleger *et al.* (1999); Sokolichin *et al.* (1997)). However, the interaction between the bubbles and the liquid leads to changes in the liquid turbulent kinetic energy distribution, budget and scales (Magolan & Baglietto (2019)). Therefore, considering BIT is crucial for improving the accuracy of the modelling of bubbly flows (Laborde-Boutet *et al.* (2009)). Recently, the performance of different

turbulence models for simple flows was investigated under consideration of the BIT effect. A heterogeneous bubble column flows was simulated by Liu & Hinrichsen (2014) for the evaluation the performance of the k-ε and Reynolds stress model (RSM) models. They showed that both models provide good liquid velocity results depending nevertheless on the drag and lift closures. Furthermore, they noticed that the applicability of the k-ε and the RSM models cannot be assessed in estimating the turbulence parameters due to the absence of experimental data of the turbulence quantities in the study. Colombo & Fairweather (2015) investigated the capability of different turbulence models for two-phase flows in a pipe. They compared the RSM of Naot & Rodi (1982), the RSM of Gibson & Launder (1978) and SSG RSM (Speziale *et al.* (1991)) and found that all models predict liquid velocity well compared to experimental data. Liang et al. (2016) tested the standard k-ε, RNG k-ε, Realizable k-ε and k-ω models to improve the simulation of mixing in bubble columns. They showed that the standard and Realizable k-ε models underestimate the liquid velocity in the center of the column, whereas the RNG k-ε model provides better liquid velocity results. Parekh & Rzehak (2018) compared the LRR (Launder *et al.* (1975)) and SSG (Speziale *et al.* (1991)) RSMs, as well as the SST model in a quasi-2D cylindrical geometry. They reported that there are only small differences between all models for mean liquid velocity. The reason that the RSM model generally showed similar performance to the two-equation models (i.e. k-ε, SST) in these studies may be that the studies examined simple flows. It has been in the literature found that for single-phase flows, the RSM has a higher performance for anisotropic flows (Vaidheeswaran & Hibiki (2017)) including strong flow line curvature, jets, and swirls (Khelil *et al.* (2016); Morrall *et al.* (2020); Song *et al.* (2018)). Although the advantage of the RSM model in the case of flows with anisotropy has been demonstrated in studies for single-phase flows, this approach is still questionable for two-phase flows.

Apart from BIT effects another characteristics of two-phase flows in engineering applications is that they contain complex flow fields. Bubble columns, for example, have internals to improve process efficiency. However, these internals lead to strong turbulence with complex flow patterns where voids can accumulate. For such a case, turbulence modelling is more difficult. Therefore, it has been less studied in the literature together with the effect of BIT. Tabib et al. (2008) simulated a laboratory scale bubble column with different spargers using three different turbulence models i.e. k-ε, RSM and LES.

They took the BIT into account by adding an additional term to the effective viscosity, i.e. a linear superposition of SIT and BIT, and used the model of Sato & Sekoguchi (1975). They found that the RSM shows better agreement than the k-ε model in predicting the turbulent kinetic energy profiles and the LES is successful in capturing the averaged behavior of the flow, while at some locations it slightly overpredicts the kinetic energy profiles. Ekambara & Dhotre (2010) investigated the performance of the standard k-ε, k-ω, RNG k-ε, RSM and LES models in a bubble column. For the RANS models, they considered the BIT with the model of Sato & Sekoguchi (1975).They showed that the k-ω yields a better qualitative prediction than the k-ε model for low Reynolds number and the RSM estimations are comparable with LES results and seem to give better prediction near the sparger, where the flow is more anisotropic. Laborde-Boutet *et al.* (2009) investigated the performance of the standard k-ε, RNG k-ε, and Realizable k-ε models in a full three-dimensional bubble column with internals. They considered the BIT by adding source terms to the turbulence transport equations. They reported that the standard k-ε and Realizable k-ε models predict radial profiles of the liquid axial velocity unsatisfactorily, yet, the RNG k-ε model provides much better predictions of the flow features.

Another critical point in modeling of turbulence for simple and complex flows is the availability of high-quality experimental data for validation. In particular, measured liquid velocity and turbulence data are required. For two-phase flows, optical methods like laser Doppler anemometry (LDA) (Akbar *et al.* (2012); Hosokawa & Tomiyama (2009)) or particle image velocimetry (PIV) (Shi *et al.* (2020)) provide highest accuracy for determination of liquid velocity. However, these optical techniques are limited to rather low gas content, as the increase of interfacial boundaries leads to significant scattering and reflection of the laser light. For higher gas fractions, thermal anemometer probes are often used to measure the liquid-phase velocity (Goldstein (2017)). For example, minimally invasive hot-film anemometer (HFA) probes are often used (Hibiki *et al.* (2001); Liu (1998); Shawkat *et al.* (2008)), which comprise of an electrically heated sensor element that is placed in the flow field. The heat flux from the sensor element to the fluids can be correlated to the flow velocity (Bruun (1995)). Hibiki *et al.* (2001) conducted experiments by using a double-sensor and a hot-film probe to measure void fraction, Sauter bubble diameter, interfacial area concentration and turbulence intensity in a pipe flow. They reported that the combined data from the double-sensor probe and the HFA probe provide complete

information on the time averaged local hydrodynamic parameters of two-phase flow. Shawkat *et al.* (2008) performed experiments of air-water bubbly flow in a pipe using a dual optical and HFA probe to measure the bubble characteristics and liquid-phase turbulence, respectively. However, the application of HFA to bubbly flows presents another challenge. Here, the interaction of bubbles with the sensor element of the probes leads to peaks in the measured voltage signals due to the sudden change in the heat capacity of liquid and gas. Thus, appropriate signal conditioning is required to analyze only signal parts that are unbiased and thus contain only the liquid velocity information. In this paper, we showed that the HFA signal can be corrected when combining its measurement with a phase-sensitive imaging technique, which is ultrafast electron beam X-ray tomography (UFXCT) here. UFXCT has previously proven its excellent capabilities for experimental two-phase flow studies, e.g. for bubble columns (Kipping *et al.* (2021); Möller *et al.* (2019)) and pipe flows (Banowski *et al.* (2018); Neumann-Kipping *et al.* (2020)).

As can be seen from the literature review, although today a variety of turbulence models are available, there is yet no general agreement about the choice of an appropriate RANS turbulence model, even for simple two-phase flows. Moreover, numerical and experimental studies of turbulence associated with complex flows, e.g. with vortex and jets in bubbly flows, have not been sufficiently carried out. Furthermore, in these few numerical studies, the BIT mostly was considered as linear superposition of BIT and SIT, which is questionable (Colombo & Fairweather (2015)). Thus, improvement of the detailed fluid dynamic model considering turbulence modelling is still required since it is necessary for the efficient design of industrial applications. The objective of this work is to contribute high-resolution data on liquid velocity and turbulence and to evaluate the performance of different turbulence models for complex two-phase flows. For this purpose, we compared CFD simulations with experimental data in a vertical half-constricted pipe. With the aid of the constriction, a vortex and a jet region were created. In the first part of the work, we performed single-phase simulations to assess the capabilities of turbulence modelling for complex flow fields. We then performed two-phase simulations considering BIT and evaluated different turbulence models with the conducted experiments. For the experiments, an enhanced approach for phase discrimination of the liquid velocity data measured by HFA probes is presented. Therefore, UFXCT, which is a non-invasive imaging technique that provides high temporal

and spatial resolution (Barthel *et al.* (2015); Fischer & Hampel (2010)) and HFA techniques were simultaneously applied to study bubbly two phase flows. With this combination, more comprehensive characterization of the flow could be achieved by extending the gas phase data (gas holdup, bubble size, bubble velocity) extracted from UFXCT by liquid velocity information from the HFA whose signals have been conditioned using the UFXCT data. Performance of the turbulence models was assessed on basis of comparison of radial profiles of axial velocity, radial velocity and turbulent kinetic energy with the experiments.

2 Experiments

2.1 Experimental setup

For a detailed description of the test section and experiments, the reader is referred to Neumann-Kipping et al. (2020). Figure 1a schematically shows the experimental setup that is located at the thermal-hydraulic test facility TOPFLOW. The test section is a vertical acrylic pipe with an inner diameter of $D = 53$ mm and a total length of $L = 4950$ mm. Here, a baffle-shaped flow constriction (Figure 1b) blocks half of the inner pipe cross-section at a distance $l = 2810$ mm above the gas injection. Deionized water is conveyed in upward direction by means of a volute pump (HPH 100-250, KSB, Germany) and the flow rate is measured by a Coriolis mass flow meter (Micro Motion ELITE CMF200, Emerson, ±0.2% RD). As gas phase, compressed air is injected at the bottom of the test section pipe via a capillary gas injection module (Figure 1c). The two main parts of the module are four thin injection tubes with an inner diameter of 0.8 mm and a liquid flow straightener comprising six metal sheets, respectively. The gas flow rate is measured and controlled by a mass flow controller (EL-FLOW, Bronkhorst, ±0.5% RD).

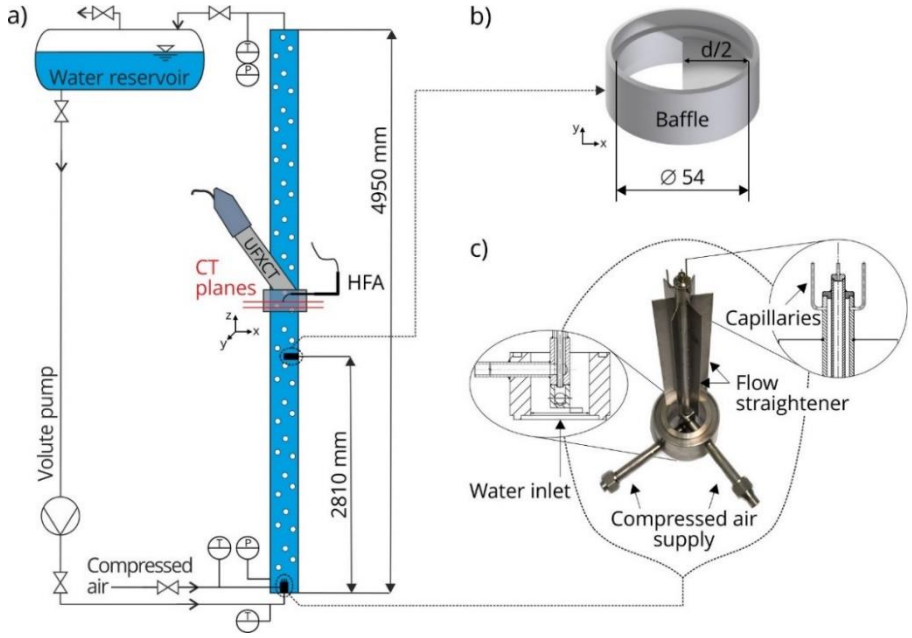

Figure 1: Sketch of a) the vertical test section, b) the baffle-shaped constriction and c) the capillary gas injection module.

All experiments were performed at constant pressure of 4 bar and liquid temperature of 30°C. Both quantities were measured at the gas injection side using an absolute pressure transmitter (Fisher-Rosemount, Emerson, ±1% RD) and a thermocouple type K (class 1, ±0.3 K after calibration (Lucas *et al.* (2016))), respectively. The major parameters of the experimental conditions are summarized in Table 1.

Table 1: Summary of flow parameters: $\dot{V}_l$ - liquid flow rate, j_l - superficial liquid velocity, Re_l - liquid Reynolds number, $\dot{V}_g$ - gas flow rate, j_g - superficial gas velocity.

Case	$\dot{V}_l$ (m³·s^{-1})	j_l (m·s^{-1})	Re_l	$\dot{V}_g$ (m³·s^{-1})	j_g (m·s^{-1})	d_B (mm)
1	8.93 x 10^{-4}	0.405	26.80 x 10^{3}	0	-	-
2	8.94 x 10^{-4}	0.405	26.82 x 10^{3}	3.33 x 10^{-5}	0.015	5.35

2.2 Ultrafast electron beam X-ray computed tomography

For general principles of computed tomography, the reader is referred to textbooks, e.g. Kak & Slaney (1988); Kalender (2011). Details of the ultrafast electron beam X-ray computed tomography (UFXCT) were described by Barthel *et al.* (2015); Fischer & Hampel (2010); Hampel *et al.* (2013). The general setup of the UFXCT scanner is shown on the left side of Figure 2. Here, a fast rotating X-ray spot is

generated by a continuously deflected electron beam. Tomographic projections are recorded with a fixed sampling frequency of 1 MHz by a circular multi-pixel dual-plane X-ray detector. Furthermore, the scanner electronics has additional input channels that allow the simultaneous sampling of further arbitrary signals, e.g. sensor signals. The acquired tomographic projections are used to reconstruct cross-sectional images of the flow. Both detector rings have an axial distance of approximate 10 mm. The UFXCT scanner provides a nominal in-plane spatial resolution of 1 mm. Using an elevator, the scanner can be moved to any position along the pipe to study the flow conditions up- and downstream of the flow constriction.

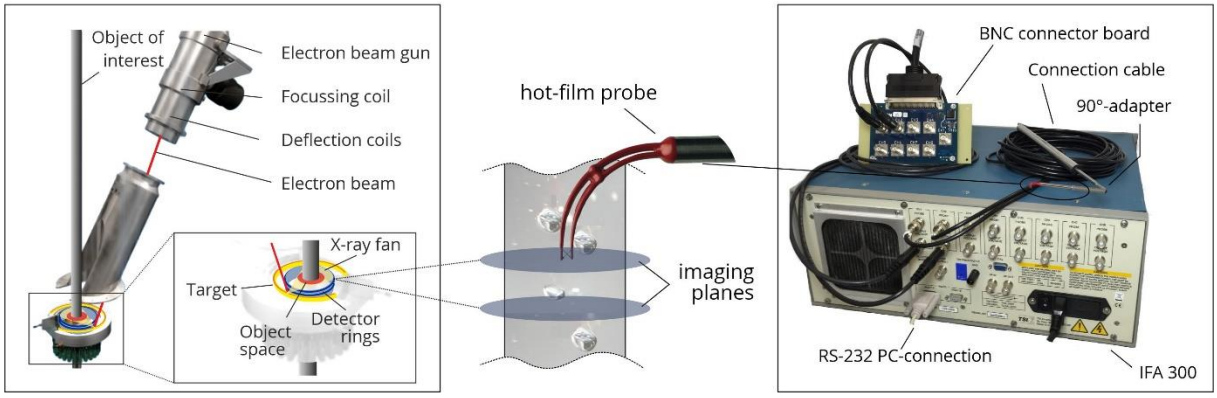

Figure 2: Combined anemometric and tomographic measurements (center) using the UFXCT scanner (left) and a dual cylindrical HFA probe 1243-20W together with the IFA 300 CTA electronics (right).

Cross-sectional images of the two-phase flow are reconstructed from the tomographic projection data by filtered back-projection method. Each image has a size of 180×180 pixels with a corresponding pixel size of 0.5 mm. Here, a pixel size smaller than the nominal spatial resolution was chosen in order to minimize discretization errors in bubble extraction from the images. An entire image stack $\mu_{i,j,k}$ contains the X-ray attenuation coefficients encoded as gray values for pixels with indices (i,j) and temporal index k. For calculation of the gas holdup, a histogram-based calibration method is applied as described by Neumann-Kipping *et al.* (2020). Here, required reference data for gas $\bar{\mu}_{i,j}^{(\mathrm{g})}$ and a liquid $\bar{\mu}_{i,j}^{(\mathrm{l})}$ are directly extracted from a two-phase flow tomographic scan $\mu_{i,j,k}^{(\mathrm{tp})}$. The gas holdup $\varepsilon_{\mathrm{i,j,k}}$ is then calculated by

$$\varepsilon_{i,j,k} = \frac{\bar{\mu}_{i,j}^{(\mathrm{l})} - \mu_{i,j,k}^{(\mathrm{tp})}}{\bar{\mu}_{i,j}^{(\mathrm{l})} - \bar{\mu}_{i,j}^{(\mathrm{g})}}. \tag{1}$$

Based on that, the ensemble averaged cross-sectional gas phase distribution $\bar{\varepsilon}_{i,j}$ and time- and space-averaged gas holdup $\bar{\varepsilon}$ are calculated according to

$$\bar{\varepsilon}_{i,j} = \frac{1}{N_k}\sum_{k=1}^{N_k} \varepsilon_{i,j,k} \tag{2}$$

and

$$\bar{\varepsilon} = \sum_{i=1}^{N_i}\sum_{j=1}^{N_j} w_{i,j}\bar{\varepsilon}_{i,j}. \tag{3}$$

Here $w_{i,j}$ are weights encoding the fraction of pixel area inside the pipe cross-section. Further, gas and liquid phase are discriminated by an iterative binarization method based on the concept of Banowski *et al.* (2015). Here, seed points of maximum gas holdup in $\varepsilon_{i,j,k}$ are used to identify pixel cluster as bubbles. By decreasing the maximum gas holdup iteratively, also small bubbles with low contrast can be identified. This is done until a termination criterion is reached, which is depending on the image frequency, the global gas holdup of the flow and noise effects, respectively. Finally, a binary data set $\varepsilon_{i,j,k}^{(\mathrm{bin})}$ containing values "1" and "0" for gas and liquid phase is obtained by the algorithm. In addition, the axial gas phase velocity map $\bar{u}_{i,j}$ is calculated according to

$$\bar{u}_{i,j} = \frac{\Delta z_{i,j}}{\Delta k_{i,j}^{(\max)}} f \quad \text{where} \qquad \Delta k_{i,j}^{(\max)} = arg\,\max_{k}\left(F_{i,j,\Delta k}\right), \tag{4}$$

using the maximum of the cross-correlation function of the gas holdup

$$F_{i,j,\Delta k} = \frac{\sum_{k=1}^{N_k} \varepsilon_{i,j,k}^{(\mathrm{low})}\varepsilon_{i,j,k}^{(\mathrm{up})}}{\sqrt{\sum_{k=1}^{N_k}\left(\varepsilon_{i,j,k}^{(\mathrm{low})}\right)^2 \sum_{k=1}^{N_k}\left(\varepsilon_{i,j,k}^{(\mathrm{up})}\right)^2}}, \tag{5}$$

which is separately calculated for each pixel pair (i,j) of upper and lower scanning plane $\varepsilon_{i,j,k}^{(\mathrm{up})}$ and $\varepsilon_{i,j,k}^{(\mathrm{low})}$, respectively. The index Δk corresponds to the time-shift $\Delta t = \Delta k/f$ with f being the image frequency per scanning plane. Further, $\Delta z_{i,j}$ corresponds to the effective image plane distance map to allow the position-dependent calculation of the bubble sizes as described by Neumann *et al.* (2019).

2.3 Hot-film anemometry

For this study, a dual cylindrical probe of type 1243-20W (TSI Inc.) was used (right of Figure 2). Both sensor elements are in close proximity and "X" configuration, allowing the simultaneous measurement of axial and radial liquid velocity components. Each sensor element has a sensing area of 50.8 µm diameter and 1.02 mm length. The probe was operated using the *IFA 300 Constant Temperature Anemometer (CTA) System* (TSI Inc. – Figure 2 right). It provides an output signal U_{out} of ± 5 V that is related to the measured voltage of an internal Wheatstone bridge U_{bdg} by

$$U_{\mathrm{bdg}} = \frac{U_{\mathrm{out}}}{g} + U_{\mathrm{off}}, \tag{6}$$

where U_{off} and g are corresponding offset and gain values that are obtained by prior calibration for each sensor element (see Table 2), respectively.

The probe was calibrated using an in-house developed water circuit that uses a standard nozzle and corresponding feed lengths to create a defined uniform flow profile (ISO (5167:2003)). The differential pressure across the nozzle was simultaneously measured with the output voltage of the CTA using a LTT24 data acquisition device with 5.000 Hz and 24 bit (LTT Labortechnik Tasler GmbH). Based on that, the liquid flow rate and, thus, flow velocity, was determined. In that way, 14 liquid flow velocities in the range of $v_{\mathrm{noz}} = 0\ldots3$ m/s were set at the nozzle in order to determine the calibration function. Considering the sensor elements angle of inflow, the effective velocity

$$v_{\mathrm{eff}} = v_{\mathrm{noz}}\, cos(45°) \tag{7}$$

is correlated to the bridge voltage by

$$v_{\mathrm{eff}}^{*} = a \cdot {U_{\mathrm{bdg}}^{*}}^{2} + b \cdot U_{\mathrm{bdg}}^{*} + c \qquad \text{with} \quad v_{\mathrm{eff}}^{*} = \sqrt{v_{\mathrm{eff}}} \quad \text{and} \quad U_{\mathrm{bdg}}^{*} = {U_{\mathrm{bdg}}}^{2} \tag{8}$$

as recommended by *IFA 300* manufacturer (Incorporated (2010)). Here, a, b and c are sensor element specific calibration parameters that are listed in Table 2.

Table 2: Calibration parameter for both HFA sensor elements.

Sensor element	U_{off} (V)	g (-)	a	b	c
I	3.49	3	2.57 x 10^{-3}	5.33 x 10^{-3}	-74.28 x 10^{-3}
II	3.52	3	1.74 x 10^{-3}	17.79 x 10^{-3}	-98.18 x 10^{-3}

Measured bridge voltages as well as the fitted calibration functions are shown in Figure 3. Using Eq. (8), the coefficient of determination is 0.9996 and 0.9992 for calibration functions I and II, respectively. It should be noted that the calibration is only valid for measurements under the same conditions, especially the same temperature of the water.

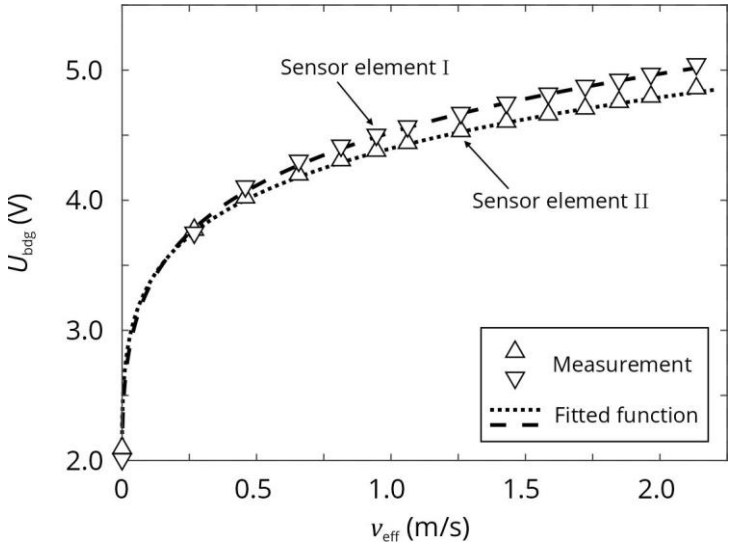

Figure 3: Calibration results showing the measured bridge voltage (Δ, ∇) and fitted calibration function ($\cdots$,---) according to Eq. (8) vs. effective velocity for both sensor elements.

To calculate effective liquid velocity $v_{\mathrm{eff,I}}$ and $v_{\mathrm{eff,II}}$ for each sensor element, the calibration function according to Eq. (8) is applied to the HFA bridge voltage signals $U_{\mathrm{bdg,I}}$ and $U_{\mathrm{bdg,II}}$, respectively. Both effective velocities are decomposed to the axial and radial velocity component u and v according to

$$u = \frac{v_\mathrm{t} + v_\mathrm{n}}{\sqrt{2}} \tag{9}$$

$$v = \frac{v_\mathrm{t} - v_\mathrm{n}}{\sqrt{2}}. \tag{10}$$

The corresponding normal component v_n and tangential component v_t of the flow velocity (referred to the HFA probes coordinate system) are calculated based on Jorgensen's equations (Jorgensen (1971)):

$$v_\mathrm{n} = \sqrt{\frac{v_{\mathrm{eff,I}}^2 - k_\mathrm{I}^2 v_{\mathrm{eff,II}}^2}{1 - k_\mathrm{I}^2\, k_\mathrm{II}^2}}, \tag{11}$$

and

$$v_\mathrm{t} = \sqrt{\frac{v_{\mathrm{eff,II}}^2 - k_\mathrm{II}^2 v_{\mathrm{eff,I}}^2}{1 - k_\mathrm{I}^2 k_\mathrm{II}^2}}. \tag{12}$$

Here, k are the yaw coefficients of both sensor elements, which are considered as the manufactures default values $k_\mathrm{I} = k_\mathrm{II} = 0.2$. Consequently, the total magnitude of the liquid velocity is given by

$$\hat{v} = \sqrt{u^2 + v^2}. \tag{13}$$

2.4 Combined anemometric and tomographic measurements

HFA signals can be conditioned by excluding data in time intervals when a gas bubble is in the vicinity or contacting the probe. Hence, the X-UFXCT scanner was positioned such that the wires of the HFA probe become visible in the upper scanning plane (see Figure 2, middle). The images from the lower plane were then screened for HFA-bubble contact. Simultaneous data acquisition is achieved by feeding the HFA probe signals to additional input channels of the UFXCT scanner electronics. Once a UFXCT scan is started, the HFA signals are sampled simultaneously with each tomographic projection (sampling interval $\tau_s = 1$ µs). Thus, precise assignment of the velocity signals to each tomographic image is possible. Each UFXCT input channel provides a measurement range of ± 5 V and a dynamic range of 12 bit, which corresponds to a resolution of the HFA signals of 2.44 x 10^{-3} V. It should be noted that although the HFA probe is operated using the *IFA 300 CTA* electronics, measurement signals are solely acquired using the additional input channels of the UFCXT scanner electronics.

The experimental procedure for simultaneous measurements was as follows. At first, liquid and gas flow rates were set according to the cases shown in Table 1. To reach stable operating conditions, a waiting period of about 30 min was observed. After that, simultaneous anemometric and tomographic measurements were performed for four radial positions of the HFA probe $r/R \approx$ (0; 0.26; 0.52; 0.78) with a distance of $\Delta x = 7$ mm, as depicted in Figure 4. In this study, the UFXCT imaging speed was set to 1,000 images per second and plane (time per image $\tau_f = 1000$ µs) for case 2 (see Table 1). This procedure was repeated for four axial positions $Z = -60$ mm, 50 mm, 100 mm and 200 mm of the HFA sensor elements as well as the upper UFXCT scanning planes with respect to the center of the flow constriction. Considering the axial pitch of both UFXCT planes, the flow was additionally imaged at $Z = -70$ mm, 40 mm, 90 mm and 190 mm by the lower scanning plane. The scanning time for each position was 15 s.

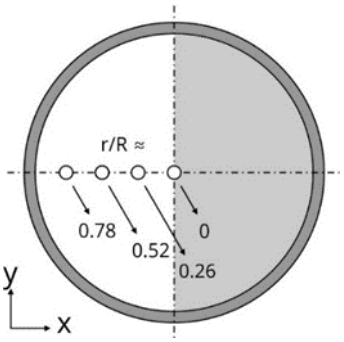

Figure 4: Radial measurement positions of the HFA probe. The gray side of the pipe cross-section indicates the position of the flow constriction.

In order to determine a phase-indicator function that labels corresponding samples of the HFA signals to bubbly spikes according to Bruun (1995), the binary UFXCT data set $\varepsilon_{i,j,k}^{(\mathrm{bin})}$ is used to extract instantaneous information of the fluidic phase at the HFA sensor elements. The phase-indicator function $\xi = \{\xi_t\}_{t=1}^{N_t}$ is defined such that

$$\xi_t = \begin{cases} 1 & \text{liquid} \\ 0 & \text{gas bubble} \end{cases} \tag{14}$$

where t is the current time step and N_t is the total number of samples per time series. First, as the probe tip dimension (app. 1.5 × 1.5 mm) and the image pixel size (0.5 × 0.5 mm) are known, a 5 x 5 pixel

image mask is centrically fitted to the HFA probe tip position within the k-averaged gray value data set of the upper imaging plane $\bar{\mu}_{i,j}^{(\mathrm{up})}$, as shown in Figure 5.

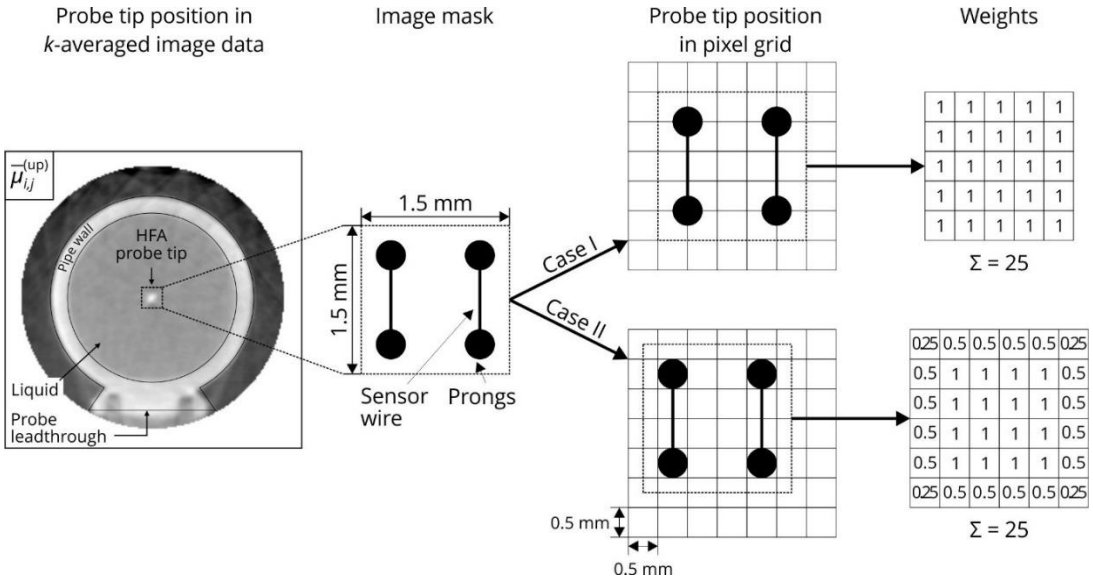

Figure 5: Sketch of the probe tip masking. From the k-averaged gray value data set $\bar{\mu}_{i,j}^{(\mathrm{up})}$ (top left) the probe tip position can be identified. A weighted mask (right) is determined, depending on the position of the sensor prongs (center).

Subsequently, the 5 x 5 pixel image mask is used to calculate the area-averaged gas fraction at the probe tip $\bar{\varepsilon}_k^{(\mathrm{tip})}$ for each image of the upper imaging plane binary data set $\varepsilon_{i,j,k}^{(\mathrm{bin,up})}$. Thus, the phase-indicator function is defined as

$$\begin{matrix} \{\xi_t\}_{t=1+(k-1)\tau^*}^{t=k\tau^*} = 1 \\ \{\xi_t\}_{t=1+(k-1)\tau^*}^{t=k\tau^*+(\tau_r/\tau_s)} = 0 \end{matrix} \quad \text{for} \quad \begin{matrix} \bar{\varepsilon}_k^{(\mathrm{tip})} = 0 \\ \bar{\varepsilon}_k^{(\mathrm{tip})} > 0. \end{matrix} \quad \text{where} \quad \tau^* = \frac{\tau_f}{\tau_s} \tag{15}$$

Here, τ_r is the characteristic response time of the *IFA 300 CTA* electronics and was found to be 3.5 ms by prior calibration. Figure 6 schematically summarizes the extraction of the phase-indicator function. Here, a typical bubble-probe interaction is shown for the HFA signal and UFXCT image data, respectively.

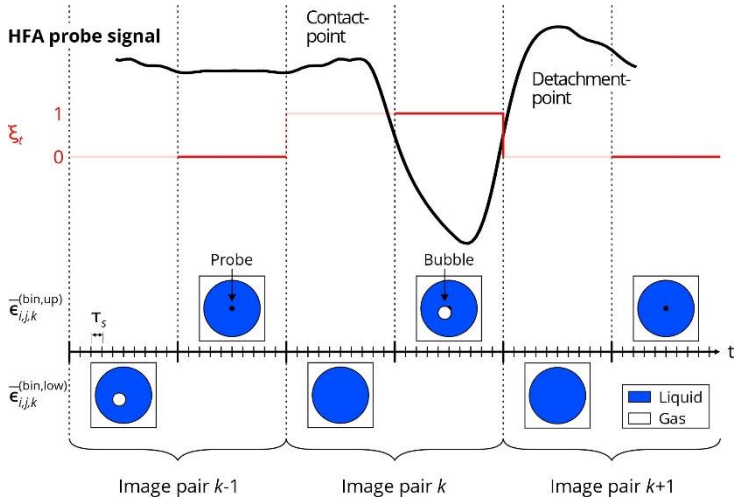

Figure 6: Schematic description of the phase-indicator function extraction from UFXCT image data.

At image pair k-1 the bubble approaches the probe tip as can be seen from the lower imaging plane binary data set $\varepsilon_{i,j,k-1}^{(\mathrm{bin,low})}$. The bubble attaches the probe at image pair k as seen from the upper imaging plane $\varepsilon_{i,j,k}^{(\mathrm{bin,up})}$. In this simplified case, the bubble already detached the probe tip at image pair k+1. Since the UFCXT image data is consecutively recorded, the maximum uncertainty of bubble attachment and detachment point is one image. Thus, each HFA sample that was recorded during image pair k is marked as bubble contact. It should be note that for simplification, the response time is excluded ($\tau_r = 0$) from the schematic indicator function in Figure 6.

A residual uncertainty of the determined phase-indicator function results from the two different sampling intervals of the HFA and the UFXCT. Thus, the determined point of contact has a maximum uncertainty of one image pair or 1 ms in this study, if the bubble contacts with the probe tip shortly after frame k-1. This might also result from the limited resolution of the UFXCT scanner and thus, the limited discrimination between liquid and gas bubbles during the binarization of the image data. However, the resulting uncertainty is rather low compared to the characteristic response time of the CTA system and has therefore no significant impact on the calculated mean velocity.

Figure 7 shows a typical velocity signal measured by the HFA probe as well as the extracted indicator function (blue color). Corresponding bubble-probe interactions and thus removed signal parts, are marked in red color.

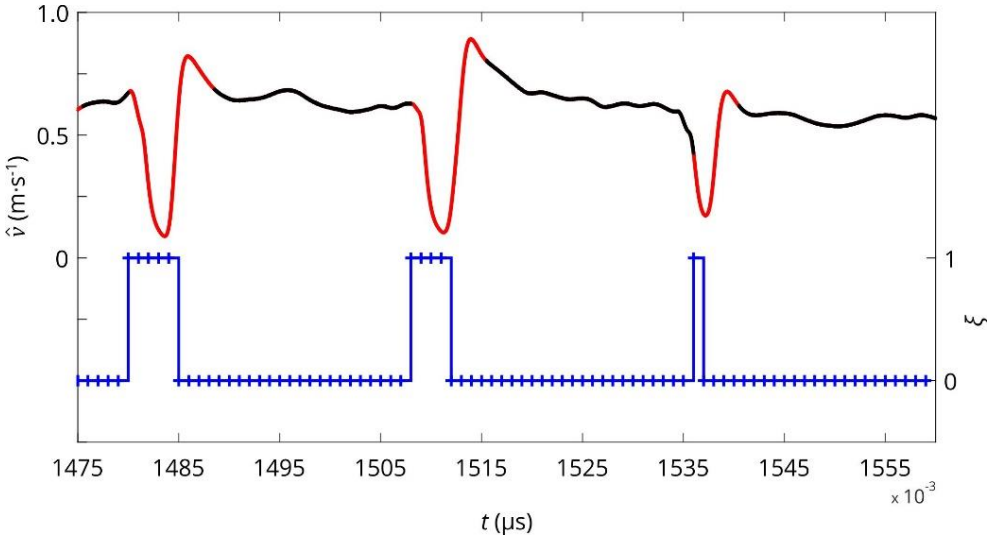

Figure 7: Typical HFA velocity signal $\hat{v}$ (top) and corresponding phase-indicator function ξ (bottom) extracted from case 2, r/R = 0 (bubble-probe interactions are marked in red color).

Using the indicator function ξ_t, statistical parameters of the liquid velocity are calculated for the two-phase flow measurement signals. The mean axial velocity $\bar{u}$ and radial velocity $\bar{v}$ components are given by

$$\bar{u} = \frac{1}{\sum_{t=1}^{N_t} \xi_t} \sum_{t=1}^{N_t} u_t \xi_t \tag{16}$$

$$\bar{v} = \frac{1}{\sum_{t=1}^{N_t} \xi_t} \sum_{t=1}^{N_t} v_t \xi_t. \tag{17}$$

The turbulent fluctuation of axial and radial velocity component $u'u'$ and $v'v'$ are defined by

$$\overline{u'u'} = \frac{1}{\sum_{t=1}^{N_t} \xi_t} \sum_{t=1}^{N_t} (\bar{u} - u_t)^2 \tag{18}$$

$$\overline{v'v'} = \frac{1}{\sum_{t=1}^{N_t} \xi_t} \sum_{t=1}^{N_t} (\bar{v} - v_t)^2. \tag{19}$$

Moreover, the shear stress $\overline{u'v'}$ is calculated by

$$\overline{u'v'} = \frac{1}{\sum_{t=1}^{N_t} \xi_t} \sum_{t=1}^{N_t} (\bar{u} - u_t)(\bar{v} - v_t). \tag{20}$$

Finally, the turbulent kinetic energy k is defined by

$$k = \frac{1}{2}(\overline{u'u'} + 2\overline{v'v'}). \quad (21)$$

Removing bubble-probe interactions from the measured velocity signal results in gapped time series as there is no liquid velocity information available. Hence, gaps are treated by a shape-preserving piecewise cubic spline interpolation, to allow for further signal evaluation.

3 Numerical setup

3.1 General remarks

The 3D geometry was defined as a vertical half tube using a symmetry XZ-plane and the flow domain was modelled from 1.5 m upstream to 1 m downstream of the constriction (Figure 8). The reason for this is that during the experiment it was observed that the flow is nearly symmetrical to the central XZ-plane and is almost fully developed at $Z = -1.5$ m. The disturbance of the obstacle disappears before $Z = 0.5$ m. In order to precisely define the inlet conditions and avoid any inlet and outlet effects, the inlet and outlet positions are set at $Z = -1.5$ m and $Z = 1.0$ m, respectively. The simulations were performed using ANSYS CFX 19.2. Boundary conditions are as follows: for single-phase RANS simulations, a liquid velocity condition (mean velocity corresponding to the superficial liquid velocity given in Table 1) and a constant pressure condition were defined as inlet and outlet, respectively. In addition, the turbulent kinetic energy and eddy dissipation resulting from the fully developed flow corresponding to the relevant velocity (Table 1) are applied as boundary conditions at the inlet. All the RANS single-phase simulations were performed at steady state condition.

For the LES simulations, a liquid velocity condition (Table 1) was set at the inlet and a constant pressure at the outlet. Time average value over duration of 15 seconds is used for the LES analysis and averaging over 5 seconds further does not bring any difference.

For two-phase flow simulations, a developed flow condition for liquid velocity, liquid turbulent kinetic energy and turbulent dissipation rate were assigned as inlet conditions, which were obtained from previous single-phase simulations and a constant pressure condition was defined as outlet condition. It is worth noting that all the investigated cases are steady-state in the physics. In the two-phase cases,

transient simulations are performed for better convergence. The flow field reaches in 5 seconds steady state and time average value over duration of 15 seconds used for the analysis.

Although considering the bubble size distribution as well as its change is important to the two-phase simulations (Liu *et al.* (2017); Liu *et al.* (2016)), a constant bubble diameter ($d_B = 5.35$ mm) was applied that was calculated from the experimental results. The reason for using a constant bubble diameter is that we have previously investigated the performance of the breakup and coalescence model of Liao *et al.* (2015) (Tas-Koehler *et al.* (2021b)), which strongly depends on the turbulence dissipation rate and found that the performance of the model decreases downstream where high turbulence changes occur. For this reason, the turbulence modelling should be investigated independently of the breakup and coalescence model, as the breakup and coalescence model will affect the turbulence when the population balance method (PBM) is used. According to the experimental results and observations, test case 2 has a homogeneous and uniform bubble size distribution, i.e. the breakup and coalescence rate is very low. This allowed us to better interpret the breakup and coalescence model using this study.

The maximum and minimum dimensionless wall distance value for the liquid phase y+ was located in the obstruction region, which was kept in the logarithmic and buffer layer, respectively. The single-phase law of wall was applied for the near wall treatment. Scalable wall function is used for ε based models and the automatic one for SST and LES. On the pipe wall, a no-slip condition was used for the liquid phase and a free-slip condition for the gas phase.

In the solver control, the turbulence numerics was set to first order and the spatial advection scheme was high resolution. The convergence criteria were set to $RMS < 10^{-5}$.

Turbulence was modelled only for the liquid phase using different RANS and LES models (Section 3.2). Here, RANS models provide additional source terms for bubble-induced turbulence (BIT) in case of two-phase simulations, where the turbulent kinematic viscosity of the gas phase was assumed to be equal to the liquid one.

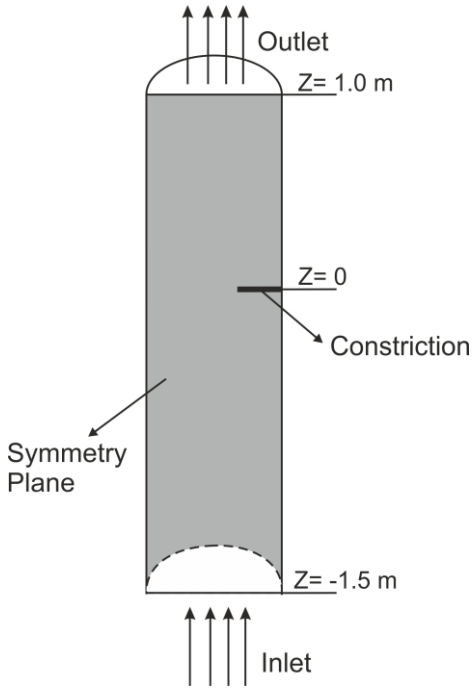

Figure 8: Schematic view of the modelling geometry (adopted from Tas-Koehler *et al.* (2021b)).

3.2 Governing equations

The single-phase flow dynamics (without heat transfer) is described by the continuity equation

$$\frac{\partial \rho}{\partial t} + \frac{\partial}{\partial x_i}(\rho u_i) = 0 \tag{22}$$

and momentum equation

$$\frac{\partial}{\partial t}(\rho u_i) + \frac{\partial}{\partial x_i}\left(\rho u_i u_j\right) = -\frac{\partial p}{\partial x_i} + \frac{\partial\left({\tau_{ij}}^{\mathrm{Lam}} + {\tau_{ij}}^{\mathrm{Turb}}\right)}{\partial x_j} + \rho g_i. \tag{23}$$

Here, ρ is the fluid density, u_i is the mean velocity component in the i-th direction, p is the pressure, ${\tau_{ij}}^{\mathrm{Lam}}$ is the laminar stress tensor, ${\tau_{ij}}^{\mathrm{Turb}}$ is the turbulence stress and t is the time.

For the two-phase flow dynamics, an Euler-Euler two-fluid model was applied in the simulations. This model defines every phase by a set of averaged conservation equations. According to this model, the modified continuity equation

$$\frac{\partial(\alpha_k \rho_k)}{\partial t} + \frac{\partial}{\partial x_i}\left(\alpha_k \rho_k u_{i,k}\right) = 0 \tag{24}$$

and momentum equation

$$\frac{\partial}{\partial t}\left(\alpha_k \rho_k u_{i,k}\right) + \frac{\partial}{\partial x_i}\left(\alpha_k \rho_k u_{i,k} u_{j,k}\right) = -\alpha_k \frac{\partial p_k}{\partial x_i} + \frac{\partial}{\partial x_j}\left[\alpha_k \left({\tau_{ij,k}}^{Lam} + {\tau_{ij,k}}^{Turb}\right)\right] + \alpha_k \rho_k g_i + M_{i,k} \quad (25)$$

are applied to solve the flow domain. Here, k is the phase indicator, α is the volume fraction and M_i is the source term, which includes the interfacial forces i.e. drag, lift, turbulent dispersion, wall lubrication and virtual mass. Mathematical expressions for the individual forces are to be found in Tas-Koehler *et al.* (2021b). All closures for interfacial force coefficients and BIT source terms are summarized in Table 3.

Table 3: Applied models for the two-phase flow simulations.

	Term	Reference	Mathematical description
Interfacial force	Drag	Ishii & Zuber (1979)	$C_D = max\left[C_{Dsphere}, min\left(C_{Dellipse,}, C_{Dcap}\right)\right]$ $C_{Dsphere} = \frac{24}{Re_B}\left(1 + 0.1{Re_B}^{3/4}\right), C_{Dellipse} = \frac{2}{3}\sqrt{Eo}, C_{Dcap} = \frac{8}{3}$
	Lift	Tomiyama *et al.* (2002)	$C_L = \begin{cases} min[0.288tanh(0.121Re), f(Eo_\perp)] & Eo_\perp < 4 \\ f(Eo_\perp) & 4 < Eo_\perp < 10 \\ -0.27 & 10 < Eo_\perp \end{cases}$ $f(Eo_\perp) = 0.00105{Eo_\perp}^3 - 0.0159{Eo_\perp}^2 - 0.0204Eo_\perp + 0.474$ $Eo_\perp = \frac{g(\rho_l - \rho_g){d_\perp}^2}{\sigma}, \; d_\perp = d_B\sqrt[3]{1 + 0.163\, Eo^{0.757}}$
	Turbulent dispersion	Burns *et al.* (2004)	Favre averaging the drag force, the constant $C_{TD} = 1.0$
	Wall lubrication	Hosokawa *et al.* (2002)	$C_W(y) = f(Eo)\left(\frac{d_B}{2y}\right)^2, \quad f(Eo) = 0.021Eo$
	Virtual mass	Auton *et al.* (1988)	Constant coefficient $C_{VM} = 0.5$
Turbulence	Liquid BIT for RANS	RANS, LES Ma *et al.* (2017)	$S_K = C_I F_D\left(u_g - u_l\right), \;\; S_\varepsilon = \frac{C_\varepsilon}{\tau} S_K, \quad S_\omega = \frac{1}{C_\mu k} S_\varepsilon - \frac{\omega}{k} S_K$ $\tau = \frac{d_B}{\left\|u_g - u_l\right\|}, \quad C_I = min\left(0.18Re_B^{0.23}, 1\right), \quad C_\varepsilon = 0.3C_D$
		Ma *et al.* (2020)	$S_{R;ij} = b_{ij}^* S_k$ $= \begin{bmatrix} \underbrace{min(0.67 + 0.67exp(370Re_B^{-1.2}), 2)}_{b_{11}^*} & 0 & 0 \\ 0 & \underbrace{\frac{1}{2}(2 - b_{11}^*)}_{b_{22}^*} & 0 \\ 0 & 0 & b_{33}^* = b_{22}^* \end{bmatrix} S_k$ $S_k = min(0.18Re_B^{0.23}, 1)F_D\left(u_g - u_l\right)$

3.3 Turbulence models for RANS simulation

In the present study, the shear stress transport (SST), Re-Normalization Group (RNG) k-ε and Speziale-Sarkar-Gatski Reynolds stress model (SSG RSM) were considered for the single- and two-phase flow simulations. Standard values are used for the constants in these models, which can be found in Ansys® CFX User´s Guide. In the two-phase case, transport equations are solved for the liquid phase, while the turbulent kinematic viscosity of the gas phase is assumed to be equal to the liquid one.

The SST model (Menter (1994)) combines the advantages of the k-ε and k-ω turbulence models. For the free-stream flow, the model applies the k-ε equations and switches to the k-ω equations in the near-wall region. The selection for this turbulence model is based on the fact that this model provided good axial gas velocity predictions for different flow conditions in previous studies (Liao *et al.* (2019); Tas-Koehler *et al.* (2021a)). The RNG k-ε model was applied in this study since it contains an additional term for turbulence production and is supposedly better suited for swirling flows (Yakhot *et al.* (1992)). It has been shown in the literature that this model provides good estimations in the presence of anisotropy in the flow (Laborde-Boutet *et al.* (2009); Tas-Koehler *et al.* (2020)) and it can be used as an alternative to RSMs, which are computationally more expensive especially in case of low swirl condition (Escue & Cui (2010); Lim *et al.* (2018)). The RSM model was developed to encounter the disadvantages of k-ω and k-ε models. It solves the transport equations for the Reynolds stress components (six independent components of Reynolds stress tensor) separately depending on the Reynolds stress tensor and the dissipation rate. Thus, it needs additional computational effort compared to k-ω and k-ε models. For a detailed description of RSMs, the reader is referred to studies of Colombo & Fairweather (2015); Hassan (2017); Parekh & Rzehak (2018); Yeoh & Tu (2019). Depending on pressure-strain term, different types of RSMs exist in the literature. Among them, the SSG (Speziale *et al.* (1991)) model that applies a quadratic pressure-strain term has the capability to predict in range of basic shear flows. Further detail about the model are found in the study of Liao & Ma (2022).

3.4 Turbulence models for LES simulation

In case of LES, the majority of the turbulent length scale are resolved by low-pass spatial filtering of the Navier-Stokes equations. The filtered mass and momentum equations are as follows:

$$\frac{\partial(\rho\bar{u}_i)}{\partial x_i} = 0 \tag{26}$$

$$\frac{\partial}{\partial t}(\rho\bar{u}_i) + \frac{\partial}{\partial x_j}\left(\rho\bar{u}_i\bar{u}_j\right) = -\frac{\partial\bar{p}}{\partial x_i} + \frac{2\partial\left(\mu\bar{S}_{ij}\right)}{\partial x_j} - \frac{\partial\left(\tau_{ij}\right)}{\partial x_j} \tag{27}$$

where $\bar{u}_i$ is the filtered velocity component in the i-th direction, $\bar{p}$ is the filtered pressure.

The filtered strain rate tensor $\bar{S}_{ij}$ and the unknown subgrid-scale (SGS) stress tensor τ_{ij} are calculated according to

$$\bar{S}_{ij} = \frac{1}{2}\left(\frac{\partial \bar{u}_j}{\partial x_i} + \frac{\partial \bar{u}_i}{\partial x_j}\right) \tag{28}$$

and

$$\tau_{ij} = \rho\left(\overline{u_i u_j} - \bar{u}_i \bar{u}_j\right), \tag{29}$$

respectively. In this model, large eddies of turbulent flow are directly resolved and only the small eddies are modelled via SGS models. Most of the available models apply an eddy viscosity model to calculate the SGS tensor

$$\tau_{ij} = 2\mu_t \bar{S}_{ij} + \frac{1}{3}\delta_{ij}\tau_{kk} \tag{30}$$

where μ_t is the SGS eddy viscosity. To determine the SGS eddy viscosity, different models have been proposed in the literature such as Smagorinsky (Smagorinsky (1963)), dynamic (Germano *et al.* (1991); Lilly (1992)) and wall-adapting local eddy viscosity (WALE) (Nicoud & Ducros (1999)). Deen *et al.* (2001) investigated the gas-liquid turbulence flow in a bubble column using Smagorinsky SGS model and obtained better quantitative agreement with experimental data of the mean and fluctuating velocities than the k-ε model. Dhotre *et al.* (2008) studied the gas-liquid flow in a bubble column with two SGS models, i.e. standard Smagorinsky SGS model and Dynamic Model. They showed that both models perform quite well and provide almost similar results. Liu *et al.* (2020) investigated the adaptiveness of different SGS models, i.e. Smagorinsky, Dynamic and WALE, on the two-phase flow and reported that the Dynamic Model and the WALE model with a model constant $C_W = 0.325$ give reasonably better agreement with the time-averaged experimental data of both the gas and liquid velocity. In this study, we also investigated the performance of aforementioned three SGS models for single-phase flow. For the Smagorinsky model, the effect of the constant (C_S) was investigated additionally.

It is important to mention that the LES modelling is more accurate than the RANS modelling since the large eddies contain most of the turbulence energy that is responsible for most of the momentum transfer and mixing. However, it is computationally more expensive compared to RANS modelling. Detailed information about the LES and SGS models can be found in the literature (Höhne (2014); Yang (2015)).

3.5 Mesh independence studies

A hexahedral mesh was used to discretize the flow domain in the present study. Figure 9 shows four different meshes with 126 x 10^3 elements (mesh 1, subfigure a), 1.2 x 10^6 elements (mesh 2, subfigure b), 7.3 x 10^6 elements (mesh 3, subfigure c) and 20.6 x 10^6 elements (mesh 4, subfigure d). The information of cell size in the vertical and lateral direction is provided in Table 4.

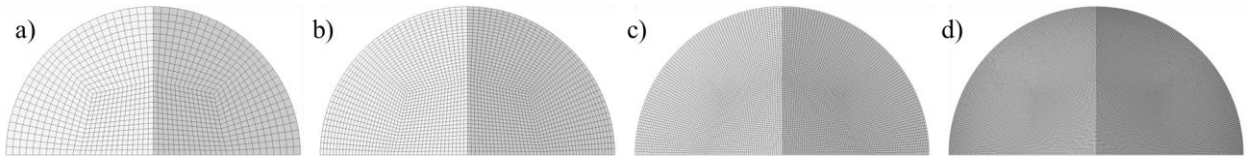

Figure 9: Mesh views: a) mesh 1 b) mesh 2 c) mesh 3 and d) mesh 4.

Table 4: Details on cell size in different meshes

	mesh 1	mesh 2	mesh 3	mesh 4
Δ_X (Δ_Y) [mm]	ca. 8 ~ 12	ca. 5 ~ 6	ca. 2.4 ~ 3.5	ca. 1.6 ~ 2.4
Δ_Z [mm]	20	5	5 (upstream) 2.5 (downstream)	5 (upstream) 2.5 (downstream)
y^+	ca. 27~60	ca. 12~40	ca. 5~22	ca. 2~8

Figure 10 shows the turbulent kinetic energy (TKE) (obtained by SST) in the radial (X) direction for increasing mesh densities. Upstream of the constriction $Z = -60$ mm, the TKE is independent of the mesh. The effect of the mesh refinement is largely noticeable downstream the constriction where the flow is highly complex. This mesh sensibility to the flow complexity is in line with that previously reported by Liao *et al.* (2019); Tas-Koehler *et al.* (2020); Tas-Koehler *et al.* (2021b).

The average relative change in TKE for position $Z = 50$ mm (which has the largest difference between mesh 2 and mesh 3 compared to other positions) is about 90% between mesh 1 and mesh 2, 17% between mesh 2 and mesh 3, and 5% between mesh 3 and mesh 4. Although mesh 3 is better compared to mesh 2, the computational cost increases 14 times when mesh 3 is used instead of mesh 2. Moreover, the computational cost for the SSG RSM or LES models is even higher than for the SST model. Furthermore, two-phase flow simulations also require a much higher computational effort. For these

reasons, we chose mesh 2 for the simulations to reduce the overall computational effort for this study. The LES results obtained by the four meshes are compared as well and similar conclusion can be drawn.

It is important to note that the bubble size and mesh size are similar in the two-phase flow simulations in the study. Regarding the relationship between mesh size and bubble size in the Euler-Euler model, Liao *et al.* (2020) and Liu & Li (2018) report from their Euler-Euler/RANS and Euler-Euler/LES simulations of a vertical pipe and a bubble column that the mesh size needs not be larger than the bubble size.

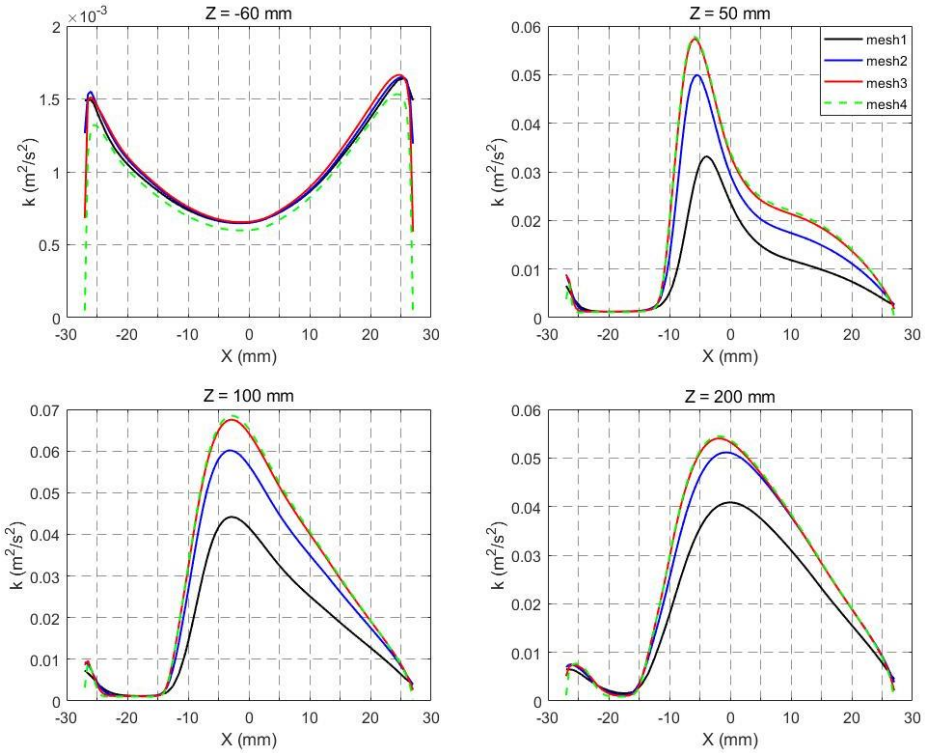

Figure 10: Effect of grid refinement on the TKE (single phase, SST).

4 Results

4.1 Single phase simulations

4.1.1 RANS simulations

For single-phase flow simulations, the capability of the SST, RNG k-ε and SSG RSM models were evaluated against the experimental results. Figure 11 shows radial profiles of the axial velocity u for different axial positions along the flow direction (Z). The obstacle is located at $Z = 0$ mm. Turbulent

flow in a pipe has a typical power-law velocity profile, which is symmetrical about the axis and has a plateau there. As the flow approaches the obstacle, the velocity on the obstacle side (right in the subfigures) decreases while the other side (left in the subfigures) increases correspondingly. The obstruction gives rise to a large gradient at the border of the obstacle ($X = 0$ mm), which recovers gradually downstream of the obstruction, see from $Z = 50$ mm to 200 mm in Figure 11. For all Z positions, the turbulence models provide similar predictions. Upstream of the constriction $Z = -60$ mm, all the turbulence models underestimate the axial velocity compared to experimental results. For $Z = 50$ mm and $Z = 100$ mm, all turbulence models predict the axial velocity well. For $Z = 200$ mm, the predictions either underestimate or overestimate the velocity u, indicating that the recovering speed is underestimated.

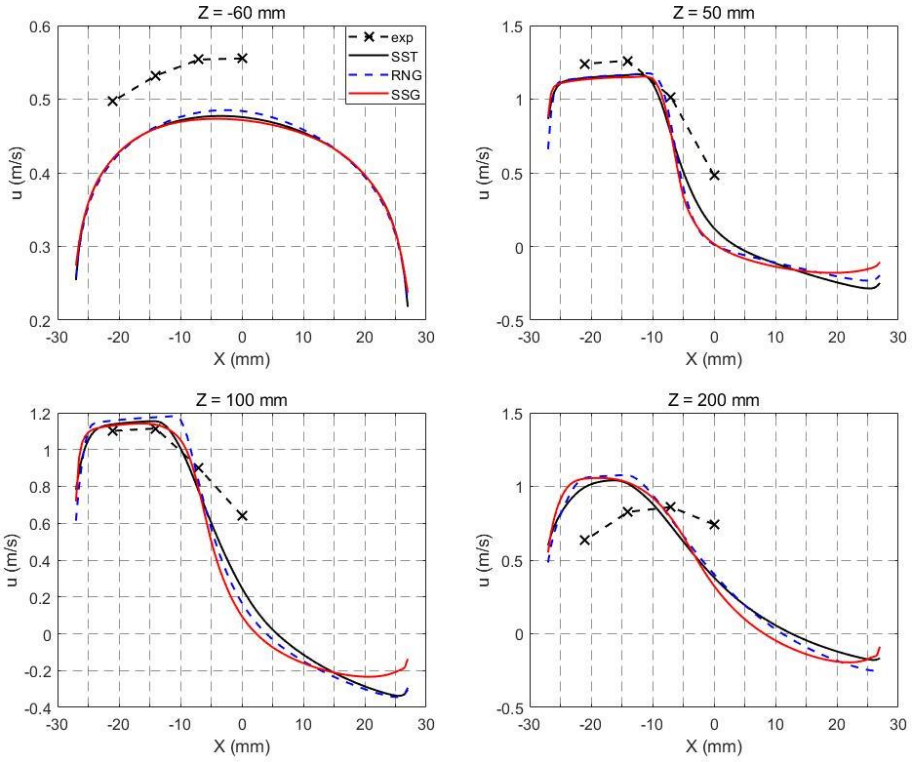

Figure 11: Axial velocity u for different turbulence models at various axial positions in single-phase flow simulations.

Figure 12 presents radial profiles of the radial velocity v for different axial positions. In the fully-developed region before the obstacle ($Z < 0$), the flow perpendicular to the main direction is rather weak, nevertheless, it should also take a parabolic profile as the simulation indicates. At $Z > 0$, because of the blockage of the obstacle the velocity in the free half cross section increases significantly, although

it is still quite low (v_{max}~0.12 m/s). This is consistent with the change of the axial velocity as discussed above. In general, the disturbance on velocity profiles is captured by the numerical model, which gives a minimum around $X = 0$ mm, however, the velocity magnitude behind the obstacle up to $Z = 200$ mm is obviously overpredicted. For $Z = -60$ mm, the simulations results are overestimated compared to the experiments. However, it is important to note that magnitudes of the radial velocities are very small here. Unlike, the predictions of the radial velocity in the half cross section free of obstacle are highly underestimated at $Z = 50$ mm, $Z = 100$ mm and $Z = 200$ mm. In addition, for $Z = 100$ mm, the RNG k-ε and SSG models predict velocity v almost the same over the whole cross section, whereas they predict it differently between -10 mm $< X <$ 30 mm for $Z = 200$ mm. The difference between the SST and other two models is already observable at $Z = 100$ mm. The reason for different model predictions can be explained in more detail with Figure 13, which shows the streamlines of the velocity for -250 mm $< Z <$ 250 mm.

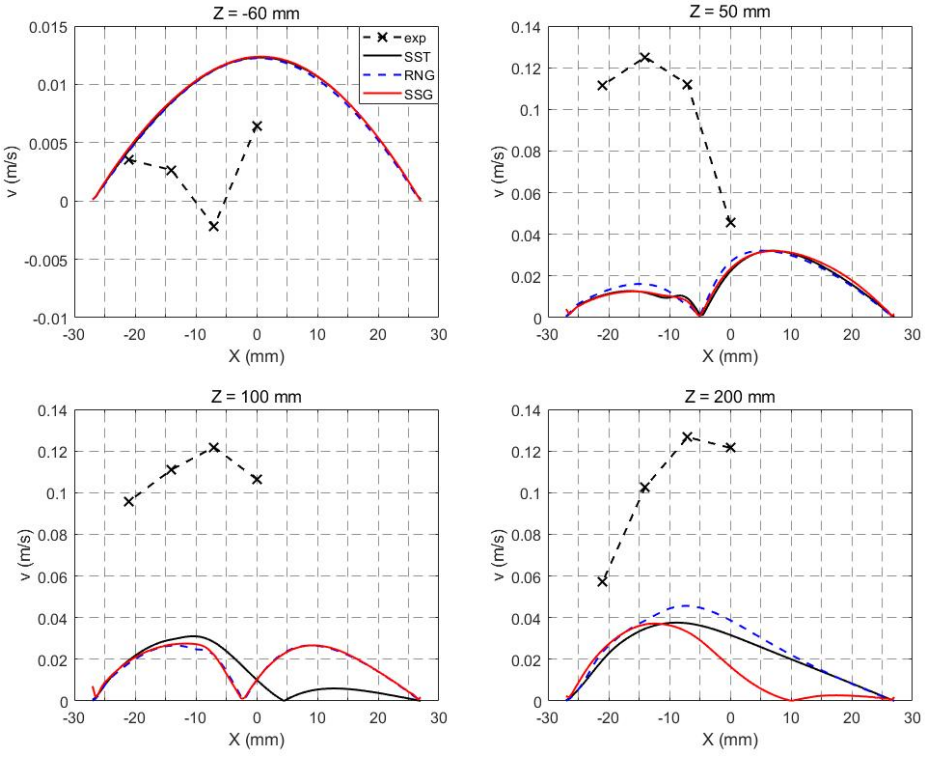

Figure 12: Radial velocity v for different turbulence models at various axial positions in single-phase flow simulations.

As can be seen in Figure 13, the streamlines are straight and uniform upstream of the constriction and all model predictions agree with each other. However, downstream of the constriction, a vortex region develops directly behind the obstacle. This vortex region is captured by all the turbulence models. However, the size and center of the vortex region changes depending on the turbulence model, which affects the predictions of radial velocity profiles in particular the velocity v, which is sensitive to the recirculation effects. In general, the vortex region predicted by the SST model is the smallest while by the SSG RSM model is the largest. The smaller that vortex is the faster the axial velocity recovers. Furthermore, a jet region is present on the unconstructed side of the pipe. With the diffusion of the jet toward the pipe center, i.e. $X = 0$, the parabolic velocity profile will be recovered. The comparison in Figure 11 shows that the speed of diffusion is underpredicted, which indicates an overprediction of the recirculation zone by all turbulence models.

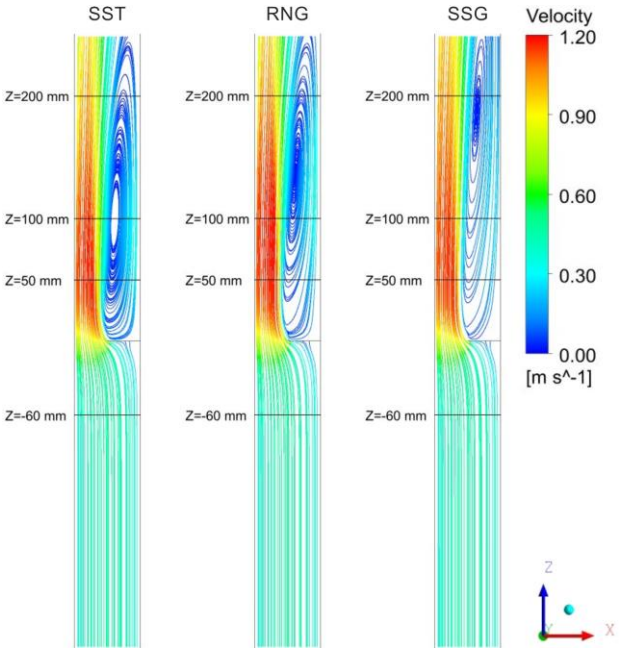

Figure 13: Streamlines obtained with different turbulence models.

Figure 14 shows radial profiles of the turbulent kinetic energy (TKE) for different axial positions. Whereas the RNG k-ε and SSG models give slightly better results compared to SST model, all the models overestimate the TKE at $Z = -60$ mm. For $Z = 50$ mm, the SSG model provides the best TKE prediction. For $Z = 100$ mm, the RNG k-ε and SSG models predict the TKE better than the SST model. For $Z = 200$ mm, all the turbulence models give similar results, yet they either underestimate or

overestimate the TKE. The slightly better performance of the SSG model may result from the direct computation of the Reynolds stresses and its capability of capturing the anisotropy.

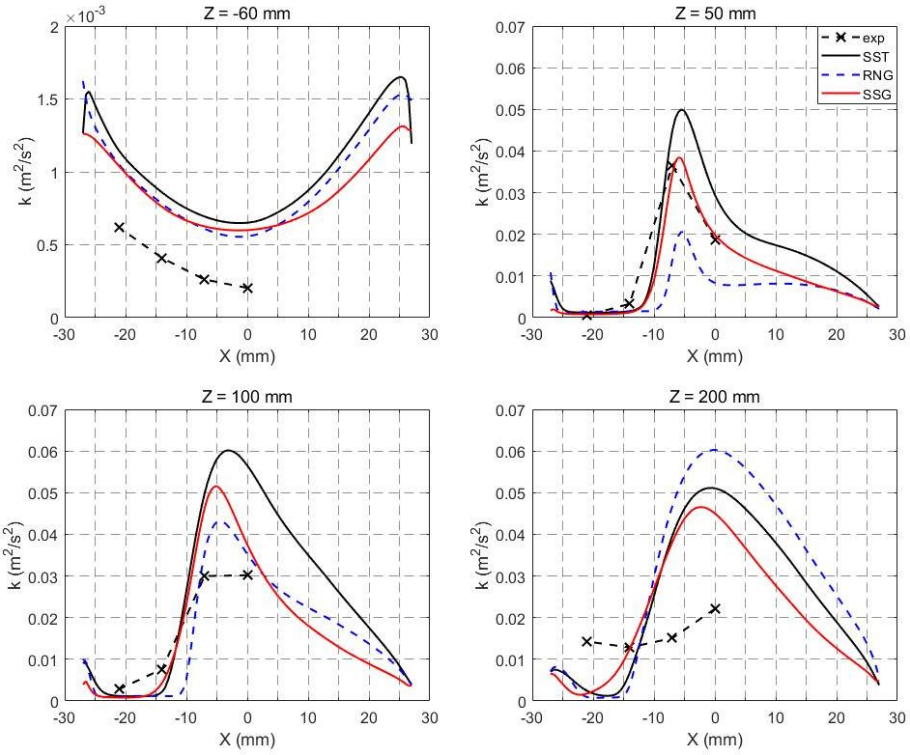

Figure 14: TKE distribution for different turbulence models at different axial positions in single-phase flow simulations.

4.1.2 LES simulations

LES models are able to predict instantaneous flow characteristics and directly resolve the large eddies of turbulence. The capabilities of different LES sub-grid models were also investigated. The LES models are also compared with the SSG model as it gives better TKE predictions at $Z = 50$ mm and $Z = 100$ mm (Figure 14). A transient simulation by applying the LES scale-resolving turbulence model was carried out for 15 s real time with a time step of $\Delta t = 0.001$ s. Figure 15 shows the time-averaged axial velocity for different models. For $Z = -60$ mm, it is clear that LES models give better predictions of velocity u compared to SSG model. Among the applied LES models, the Smagorinsky model provides the best results. For $Z = 50$ mm, both the LES and SSG models provide similar results, which are slightly underestimated compared to experimental results. For $Z = 100$ mm, the results of the SSG model agree well with experiments, whereas the results of the LES models are slightly underestimated.

For $Z = 200$ mm, there are deviations between the experimental and numerical results for both the SSG and LES models. Nevertheless, both simulation and experiment captures the momentum diffusion due to shear stresses, which is in the direction of decreasing velocity. As a result, the velocity in the open half cross section (-30 mm $< X < 0$ mm) decreases where in the blocked half (0 mm $< X < 30$ mm) increases. The comparison shows that the LES models overpredict the rate of diffusion, while the RANS ones under-predict as discussed above. In other words, the eddy viscosity controlling the shear stress is overpredicted by the LES models in particular in the circulation region behind the obstacle.

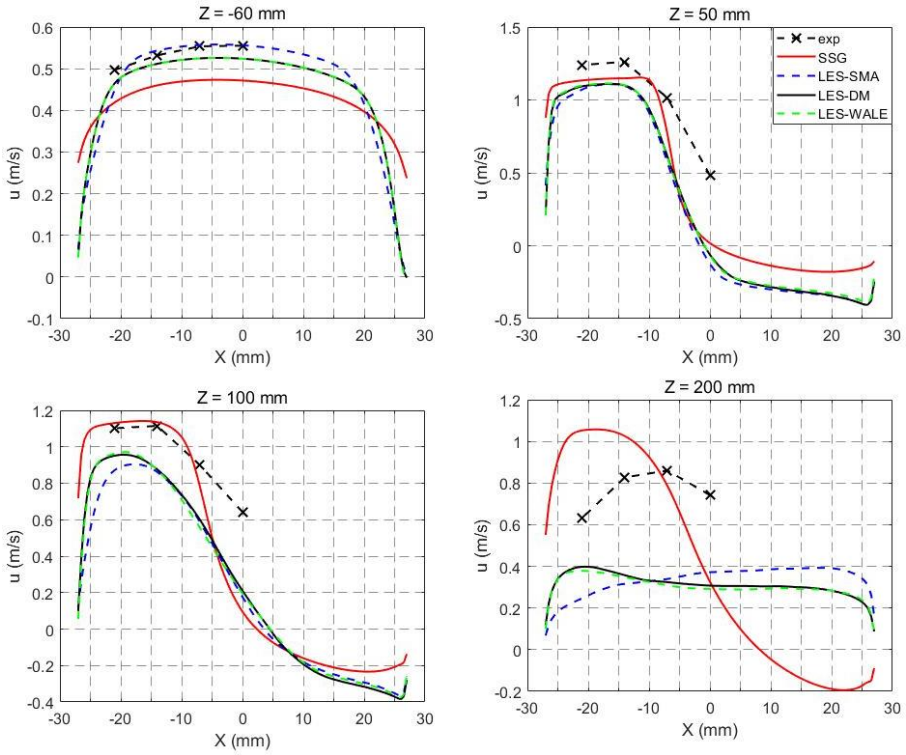

Figure 15: Axial velocity u for different LES models and SSG model at different axial positions in single-phase flow simulations.

In terms of radial velocity, the LES models improved the predictions downstream of the constriction as shown in Figure 16. Among them, the Smagorinsky model predicts the velocity v slightly better.

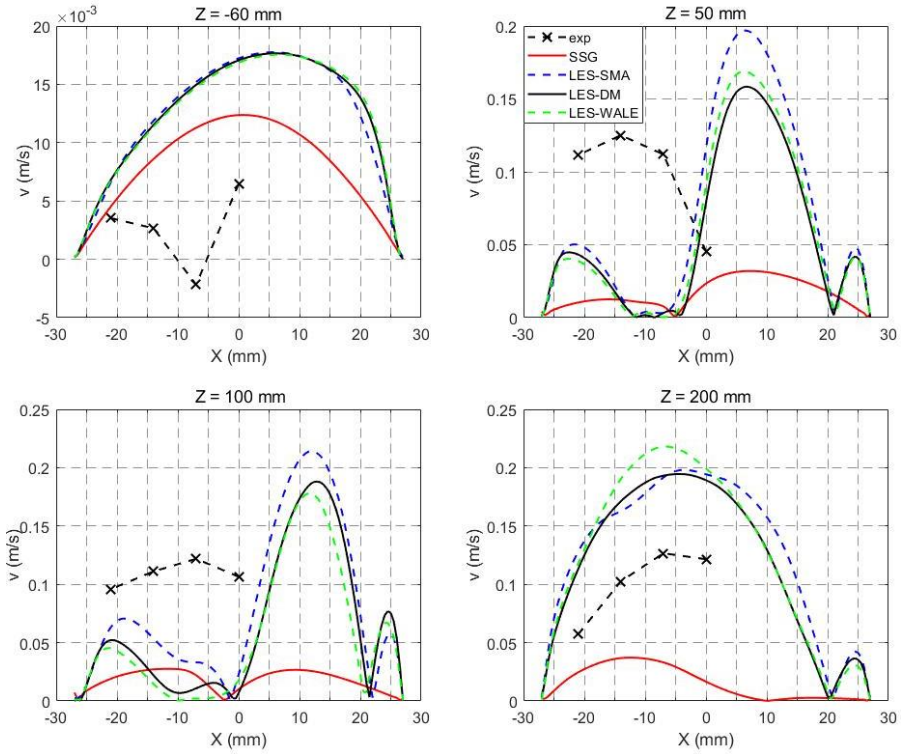

Figure 16: Radial velocity v for different LES models and SSG model at different axial positions in single-phase flow simulations.

For the Smagorinsky model, the SGS eddy viscosity (Eq. 30) is calculated using by

$$\mu_t = \rho(C_S\Delta)^2|S|. \tag{31}$$

Here, S is the characteristic filtered rate of strain, Δ is the filter width

$$\Delta = \left(\Delta_i\Delta_j\Delta_k\right)^{1/3} \tag{32}$$

and C_S is the Smagorinsky constant that generally varies between 0.08 and 0.22 for single-phase flows (Zhang *et al.* (2006)). Canuto & Cheng (1997) found that although $C_S = 0.11$ may look like a universal constant, it is a dynamic variable that may be varied between $C_S = 0.11$-0.22 depending on the flow. Thus, the effect of the C_S was also investigated since flow features changes downstream compared to upstream. As shown in Figure 17, $C_S = 0.10$ provides better axial velocity results compared to other values for $Z = -60$ mm. However, the C_S factor has very small effect on the axial velocity predictions downstream of the constriction. Nevertheless, the tendency of momentum diffusion increasing with the

viscosity and thus, C_S value is observable. It looks that a smaller value should be used for C_S in the recirculation region downstream of the obstacle.

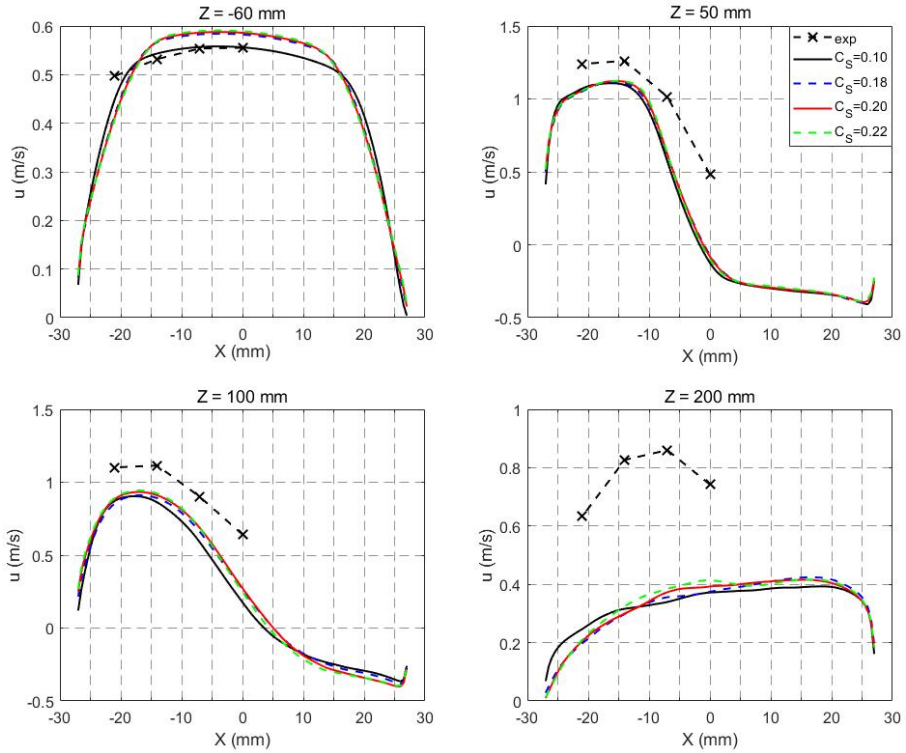

Figure 17: Axial velocity u for different C_S constants at different axial positions in single-phase flow simulations.

4.2 Two-phase flow simulations

For two-phase flow simulations, the turbulence modelling is even complicated by the relative motion between the phases. The capability of the SST, RNG k-ε and SSG RSM models were also assessed with aid of the experimental data. Turbulence modulation due to the presence of bubbles is considered by the model of Ma *et al.* (2017) for the SST and RNG k-ε models and by the model of Ma *et al.* (2020) for the SSG model. The two-phase case investigated has the same liquid volumetric flux as the single-phase case discussed above (see Table 1). Figure 18 shows radial profiles of the axial velocity u for different Z positions. For all Z positions, the results are similar to single-phase flow. The models behave similarly. Slight underprediction of the velocity magnitude upstream and momentum diffusion downstream of the constriction is observed.

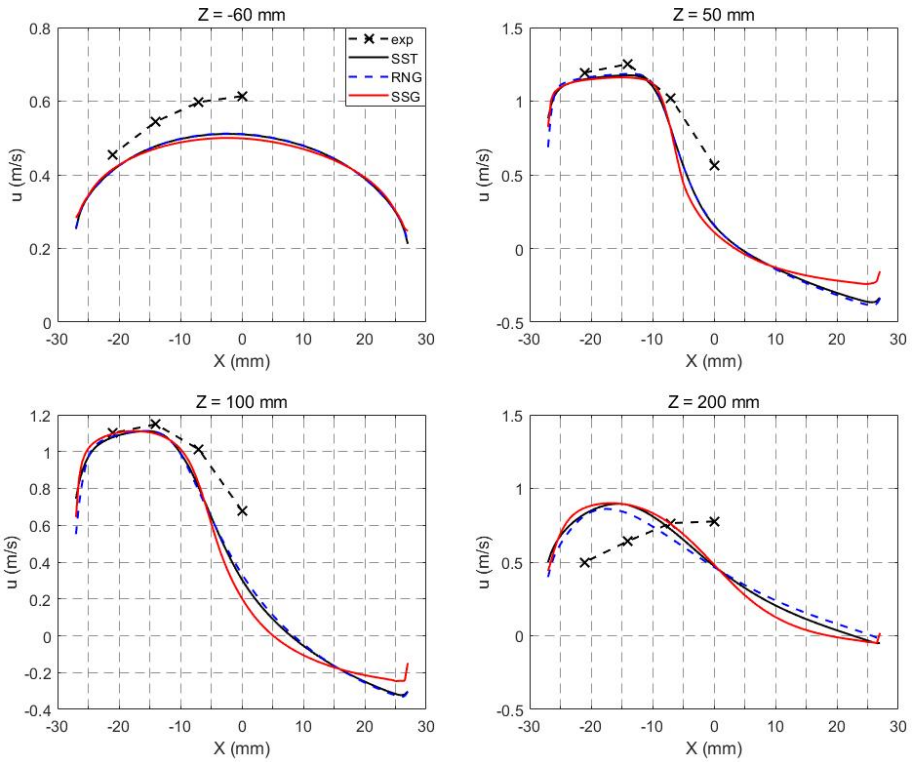

Figure 18: Axial velocity u for different turbulence models at various axial positions in two-phase flow simulations.

Figure 19 shows the radial velocity v predictions for different Z positions. The predictions for all Z positions show a similar trend to the predictions for single-phase flow. However, for $Z = 50$ mm, $Z = 100$ mm and $Z = 200$ mm, the predictions are better, i.e. they are quantitatively closer to the experimental results.

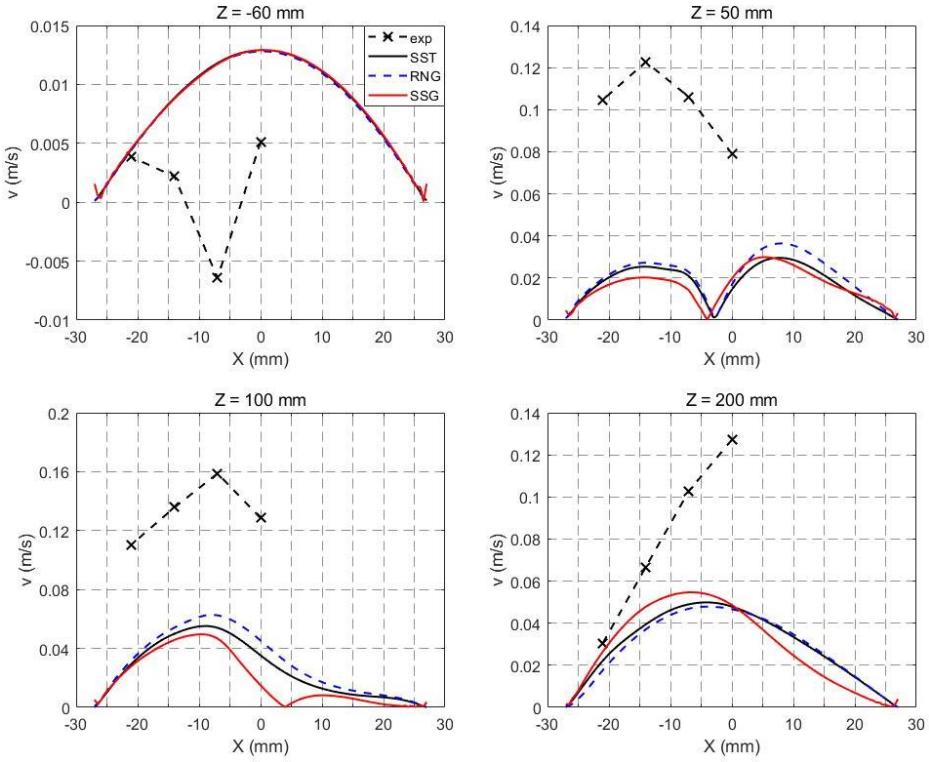

Figure 19: Radial velocity v for different turbulence models at various axial positions in two-phase flow simulations.

Considering TKE, the RNG k-ε model noticeably improves the predictions at $Z = -60$ mm as shown in Figure 20. For $Z = 50$ mm and $Z = 100$ mm, the RNG k-ε and SSG models provides similar TKE predictions at $X < -5$ mm. The difference between the predictions of these models and the experimental data increases near $X = 0$, i.e. in the middle of the pipe. Likewise, at $X > 0$ where there is a vortex region due to the constriction (Figure 13) the models provide relatively different predictions compared to each other. For $Z = 200$ mm, all the turbulence models underestimate or overestimate the TKE.

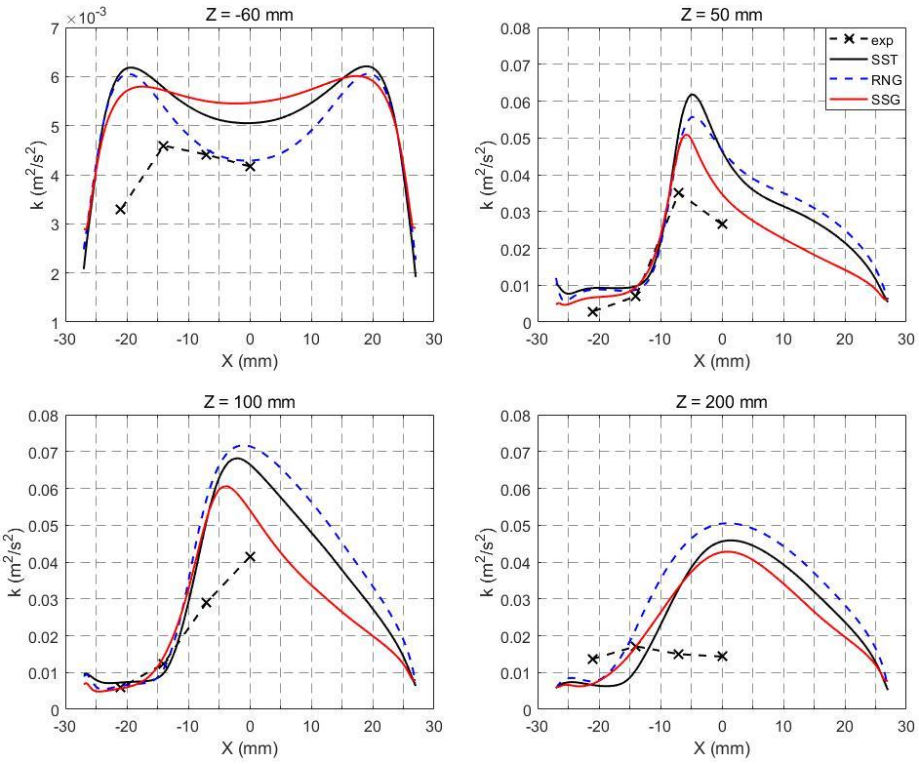

Figure 20: TKE for different turbulence models at various axial positions in two-phase flow simulations.

5 Discussion

Considering single-phase flow, slight underprediction of momentum diffusion from the obstructed to the unobstructed half of the pipe upstream the constriction and vice versa downstream is observed. On the other hand, the models are less capable to predict the radial velocity v. Although the trends in the change of radial velocity are captured at the downstream constriction, there are large discrepancies between simulations and experiments in terms of magnitude. However, as the jet effect weakens, the discrepancies between predictions and experiments decrease. Besides, the low magnitude of radial velocity v complex flow structures behind the obstacle like jets and vortices are challenging for all models. One important point is that the RNG k-ε and SSG RSM models provide similar predictions of velocity v except for $Z = 200$ mm. Further experiments for the constriction downstream are necessary to explain this. The TKE predictions agree well with the experiments for $Z = 50$ mm and $Z = 100$ mm. Among the models, the predictions of the SSG model that solves the Reynolds stresses directly provide better TKE predictions. As a result, there are discrepancies in axial velocity, radial velocity and TKE between the experimental data and the numerical results for the upstream region. One of the reasons for this could be the jet effects that could not be captured by the eddy-viscosity models RANS simulations.

In addition, the RNG k-ε model, which includes an additional term for turbulence production, shows similar performance to the SSG model. Therefore, the RNG k-ε model can be chosen instead of the SSG model for complex flow simulations, as it requires less computational effort. In terms of LES models, the Smagorinsky model provides the best axial velocity prediction for the constriction upstream. However, the capability of the Smagorisnky model is similar to the SSG model for the constriction downstream. The constant C_S, is one of the most important inputs for the Smagorinsky model. Nevertheless, in the recirculation region downstream of the obstacle it has limited effects since there the resolved large eddies are dominant. Another important point is that for $Z = 200$ mm, both RANS and LES models give unsatisfactory predictions in terms of all parameters.

The two-phase case investigated in this study is similar to the single-phase one concerning the change of velocity and turbulence passing the obstacle. It indicates that the bubbles have only a minor influence on the development of the flow conditions for such a geometry.

6 Conclusion

This paper presents a comprehensive study of single- and two-phase flow in a constricted vertical pipe with a focus on liquid velocity and turbulence. The liquid velocity was measured by means of constant temperature hot-film anemometry. Therefore, an advanced approach for conditioning of the velocity signal developed. Here, HFA measurements were combined with simultaneous ultrafast X-ray tomography scans to extract a phase-indicator function from the tomographic image data. In that way, biased signal parts of the bubble-probe contacts are effectively removed from the HFA signal. The experiments showed that the acceleration of the flow leads to an increase of the axial liquid velocity to more than twice of the upstream flow. As the flow reattaches downstream of the constriction, the peak of the radial liquid velocity shifts from the pipe wall to the center of the pipe. The interaction of the liquid jet and the recirculating flow above the constriction results in a peak of the turbulent kinetic energy close to the center of the pipe for $Z = 50$ mm and $Z = 100$ mm.

The measured axial and radial components of the liquid velocities and calculated turbulent kinetic energy were used to evaluate numerical simulations with state-of-the-art models in single- and two-

phase flows. In terms of two-phase flow modelling, this study is one of the few in the literature that considers the BIT effect in complex flows.

The capabilities of different RANS models, e.g. SST, RNG k-ε and SSG RSM as well as LES models, were investigated. For single-phase flow, all RANS models provide similar predictions for axial velocity and the predictions are generally satisfactory in comparison with experimental data. Although the RANS simulations agree well with the experiments at $Z = 50$ mm and $Z = 100$ mm, there are considerable discrepancies at $Z = -60$ mm and 200 mm. However, the LES simulation significantly improves the prediction of the axial velocity at $Z = -60$ mm. The reason for this could be the large eddies in the flow that occur at this Z position and are resolved by the LES model.

For $Z = 200$ mm, neither RANS nor LES models give good predictions. It is also important to note that there are also large differences between the predictions of the SSG RSM and LES models at this position. It can be concluded that the LES modelling performance decreases when the Z position changes from $Z = -60$ mm to 200 mm. The reason for this could be that when the flow across the obstacle, large turbulent eddies turn into small ones that cannot be modelled properly by the SGS approach.

Although the LES and SSG RSM models predict radial velocities relatively differently compared to the experimental results, the LES modelling has better performance downstream compared to the SSG RSM. However, there are still large discrepancies between LES and experimental results.

Another point is that there is a difference between the LES and SSG RSM models on the constricted side of the pipe (vortex side) with respect to both axial and radial velocities. Since the measurements were only made on the jet flow side, it is necessary to make the measurements on the vortex side to better assess the performance of the models.

For two-phase flow, the axial velocity is well captured by all RANS models and the radial velocity is better predicted than for single-phase flow. Reliable prediction of the turbulent hydrodynamics in complex geometry, which is often the case in technical applications, is still challenging for available models.

Acknowledgments

This work is funded by the German Federal Ministry for Economic Affairs and Energy (BMWi) with the grant number 1501481 on the basis of a decision by the German Bundestag.

References

Akbar, M. H. b. M., Hayashi, K., Hosokawa, S., & Tomiyama, A. (2012). Bubble tracking simulation of bubble-induced pseudoturbulence. *24*(3), 197-222. doi:10.1615/MultScienTechn.v24.i3.20

Ansys®. *Theory Guide, Release 19.2, Help System*: ANSYS, Inc.

Auton, T. R., Hunt, J. C. R., & Prudhomme, M. (1988). The Force Exerted on a Body in Inviscid Unsteady Non-Uniform Rotational Flow. *Journal of Fluid Mechanics, 197*, 241-257. doi:10.1017/S0022112088003246

Banowski, M., Hampel, U., Krepper, E., Beyer, M., & Lucas, D. (2018). Experimental investigation of two-phase pipe flow with ultrafast X-ray tomography and comparison with state-of-the-art CFD simulations. *Nuclear Engineering and Design, 336*, 90-104. doi:10.1016/j.nucengdes.2017.06.035

Banowski, M., Lucas, D., & Szalinski, L. (2015). A new algorithm for segmentation of ultrafast X-ray tomographed gas-liquid flows. *International Journal of Thermal Sciences, 90*, 311-322. doi:10.1016/j.ijthermalsci.2014.12.015

Barthel, F., Bieberle, M., Hoppe, D., Banowski, M., & Hampel, U. (2015). Velocity measurement for two-phase flows based on ultrafast X-ray tomography. *Flow Measurement and Instrumentation, 46*, 196-203. doi:10.1016/j.flowmeasinst.2015.06.006

Bruun, H. H. (1995). *Hot Wire Anemometry: Principles and Signal Analysis*. Oxford: Oxford University Press.

Burns, A. D., Frank, T., Hamill, I., & Shi, J.-M. (2004). *The Favre averaged drag model for turbulent dispersion in Eulerian multi-phase flows*. Paper presented at the 5th Iinternational Conference on Multiphase Flow, ICMF, Yokohama, Japan.

Canuto, V. M., & Cheng, Y. (1997). Determination of the Smagorinsky-Lilly constant C-s. *Physics of Fluids, 9*(5), 1368-1378. doi:10.1063/1.869251

Colombo, M., & Fairweather, M. (2015). Multiphase turbulence in bubbly flows: RANS simulations. *International Journal of Multiphase Flow, 77*, 222-243. doi:10.1016/j.ijmultiphaseflow.2015.09.003

Deen, N. G., Solberg, T., & Hjertager, B. H. (2001). Large eddy simulation of the Gas–Liquid flow in a square cross-sectioned bubble column. *Chemical Engineering Science, 56*(21), 6341-6349. doi:10.1016/S0009-2509(01)00249-4

Dhotre, M. T., Niceno, B., & Smith, B. L. (2008). Large eddy simulation of a bubble column using dynamic sub-grid scale model. *Chemical Engineering Journal, 136*(2), 337-348. doi:10.1016/j.cej.2007.04.016

Ekambara, K., & Dhotre, M. T. (2010). CFD simulation of bubble column. *Nuclear Engineering and Design, 240*(5), 963-969. doi:10.1016/j.nucengdes.2010.01.016

Escue, A., & Cui, J. (2010). Comparison of turbulence models in simulating swirling pipe flows. *Applied Mathematical Modelling, 34*(10), 2840-2849. doi:10.1016/j.apm.2009.12.018

Fischer, F., & Hampel, U. (2010). Ultra fast electron beam X-ray computed tomography for two-phase flow measurement. *Nuclear Engineering and Design, 240*(9), 2254-2259. doi:10.1016/j.nucengdes.2009.11.016

Germano, M., Piomelli, U., Moin, P., & Cabot, W. H. (1991). A dynamic subgrid-scale eddy viscosity model. *Physics of Fluids a-Fluid Dynamics, 3*(7), 1760-1765. doi:10.1063/1.857955

Gibson, M. M., & Launder, B. E. (1978). Ground Effects on Pressure-Fluctuations in Atmospheric Boundary-Layer. *Journal of Fluid Mechanics, 86*(JUN), 491-511. doi:10.1017/s0022112078001251

Goldstein, R. (2017). *Fluid Mechanics Measurements* (2nd ed.): Taylor & Francis.

Hampel, U., Krepper, E., Lucas, D., Beyer, M., Szalinski, L., Banowski, M., . . . Barth, T. (2013). High-resolution two-phase flow measurement techniques for the generation of experimental data for CFD code qualification. *Kerntechnik, 78*(1), 9-15. doi:10.3139/124.110301

Hassan, Y. (2017). An overview of computational fluid dynamics and nuclear applications In *Thermal-Hydraulics of Water Cooled Nuclear Reactors* (pp. 729–829): Elsevier.

Hibiki, T., Ishii, M., & Xiao, Z. (2001). Axial interfacial area transport of vertical bubbly flows. *International Journal of Heat and Mass Transfer, 44*(10), 1869-1888. doi:10.1016/S0017-9310(00)00232-5

Höhne, T. (2014). Scale resolved simulations of the OECD/NEA-Vattenfall T-junction benchmark. *Nuclear Engineering and Design, 269*, 149-154. doi:10.1016/j.nucengdes.2013.08.021

Hosokawa, S., & Tomiyama, A. (2009). Multi-fluid simulation of turbulent bubbly pipe flows. *Chemical Engineering Science, 64*(24), 5308-5318. doi:10.1016/j.ces.2009.09.017

Hosokawa, S., Tomiyama, A., Misaki, S., & Hamada, T. (2002). *Lateral migration of single bubbles due to the presence of wall*. Paper presented at the Proceedings of the ASME Joint U.S.-European Fluids Engineering Division Conference, FEDSM2002, Montreal, Canada.

Hossain, M. S., Hossain, M. I., Pramanik, S., & Ahamed, J. U. (2017). Analyzing the turbulent flow characteristics by utilizing k-ε turbulence model. *Eur. J. Eng. Res.Sci., 2*(11), 28–34.

Incorporated, T. (2010). *T. Incorporated, IFA 300 Constant Temperature Anemometer System, Revision D*. Retrieved from

Ishii, M., & Zuber, N. (1979). Drag Coefficient and Relative Velocity in Bubbly, Droplet or Particulate Flows. *Aiche Journal, 25*(5), 843-855. doi:10.1002/aic.690250513

ISO. (5167:2003). Measurement of fluid flow by means of pressure differential devices inserted in circular cross-section conduits running full — Part 3: Nozzles and Venturi nozzles (ISO 5167-3:2003). In. https://www.iso.org/standard/30191.html.

Jorgensen, F. E. (1971). Directional Sensitivity of Wire and Fibre-Film Probes. *DISA Inf. No. 11*.

Kak, A., & Slaney, M. (1988). *Principles of Computerized Tomographic Imaging*. New York: IEEE Press.

Kalender, W. A. (2011). *Computed Tomography: Fundamentals, System Technology, Image Quality, Applications* (3rd edn ed.). Erlangen: Publicis Erlangen.

Khelil, A., Naji, H., Loukarfi, L., Meliani, M. H., & Braikia, M. (2016). Numerical simulation of the interactions among multiple turbulent swirling jets mounted in unbalanced positions. *Applied Mathematical Modelling, 40*(5-6), 3749-3763. doi:10.1016/j.apm.2015.10.047

Kipping, R., Kryk, H., & Hampel, U. (2021). Experimental analysis of gas phase dynamics in a lab scale bubble column operated with deionized water and NaOH solution under uniform bubbly flow conditions. *Chemical Engineering Science, 229*. doi:10.1016/j.ces.2020.116056

Laborde-Boutet, C., Larachi, F., Dromard, N., Delsart, O., & Schweich, D. (2009). CFD simulation of bubble column flows: Investigations on turbulence models in RANS approach. *Chemical Engineering Science, 64*(21), 4399-4413. doi:10.1016/j.ces.2009.07.009

Launder, B. E., Reece, G. J., & Rodi, W. (1975). Progress in development of a Reynolds-stress turbulence closure. *Journal of Fluid Mechanics, 68*(APR15), 537-566. doi:10.1017/s0022112075001814

Liang, X. F., Pan, H., Su, Y. H., & Luo, Z. H. (2016). CFD-PBM approach with modified drag model for the gas-liquid flow in a bubble column. *Chemical Engineering Research & Design, 112*, 88-102. doi:10.1016/j.cherd.2016.06.014

Liao, Y., & Ma, T. (2022). Study on bubble-induced turbulence in pipes and containers with Reynolds-stress models. *Experimental and Computational Multiphase Flow*. doi:10.1007/s42757-021-0128-0

Liao, Y., Ma, T., Krepper, E., Lucas, D., & Frohlich, J. (2019). Application of a novel model for bubble-induced turbulence to bubbly flows in containers and vertical pipes. *Chemical Engineering Science, 202*, 55-69. doi:10.1016/j.ces.2019.03.007

Liao, Y., Rzehak, R., Lucas, D., & Krepper, E. (2015). Baseline closure model for dispersed bubbly flow: Bubble coalescence and breakup. *Chemical Engineering Science, 122*, 336-349. doi:10.1016/j.ces.2014.09.042

Liao, Y., Upadhyay, K., & Schlegel, F. (2020). Eulerian-Eulerian two-fluid model for laminar bubbly pipe flows: Validation of the baseline model. *Computers & Fluids, 202*. doi:10.1016/j.compfluid.2020.104496

Lilly, D. K. (1992). A proposed modification of the germano-subgrid-scale closure method. *Physics of Fluids a-Fluid Dynamics, 4*(3), 633-635. doi:10.1063/1.858280

Lim, D. C., Al-Kayiem, H. H., & Kurnia, J. C. (2018). Comparison of Different Turbulence Models in Pipe Flow of Various Reynolds Numbers. In S. R. Pedapati, W. P. K. Soon, M. S. Nasif, H. Ya, S. A. B. Sulaiman, & O. B. Mamat (Eds.), *6th International Conference on Production, Energy and Reliability 2018: World Engineering Science & Technology Congress* (Vol. 2035).

Liu, T. J. (1998). *The role of bubble size on liquid phase turbulent structure in two-phase bubbly flow*. Paper presented at the 3rd International Conference on Multiphase Flow (ICMF1998), Lyon, France.

Liu, Y. F., & Hinrichsen, O. (2014). Study on CFD-PBM turbulence closures based on k-epsilon and Reynolds stress models for heterogeneous bubble column flows. *Computers & Fluids, 105*, 91-100. doi:10.1016/j.compfluid.2014.09.023

Liu, Z., Li, B., Qi, F., & Cheung, S. C. P. (2017). Population balance modeling of polydispersed bubbly flow in continuous casting using average bubble number density approach. *Powder Technology, 319*, 139-147. doi:10.1016/j.powtec.2017.06.034

Liu, Z. Q., & Li, B. K. (2018). Scale-adaptive analysis of Euler-Euler large eddy simulation for laboratory scale dispersed bubbly flows. *Chemical Engineering Journal, 338*, 465-477. doi:10.1016/j.cej.2018.01.051

Liu, Z. Q., Qi, F. S., Li, B. K., & Cheung, S. C. P. (2016). Modeling of bubble behaviors and size distribution in a slab continuous casting mold. *International Journal of Multiphase Flow, 79*, 190-201. doi:10.1016/j.ijmultiphaseflow.2015.07.009

Liu, Z. Q., Wu, Y., & Li, B. (2020). An assessment on the performance of sub-grid scale models of large eddy simulation in modeling bubbly flows. *Powder Technology, 374*, 470-481. doi:10.1016/j.powtec.2020.07.055

Loyseau, X. F., Verdin, P. G., & Brown, L. D. (2018). Scale-up and turbulence modelling in pipes. *Journal of Petroleum Science and Engineering, 162*, 1-11. doi:10.1016/j.petrol.2017.12.019

Lucas, D., Beyer, M., Banowski, M., Seidel, T., Krepper, E., Liao, Y., . . . Ma, T. (2016). *TOPFLOW-experiments, model development and validation for the qualification of CFD-odes for two-phase flows-Final report (HZDR--077)*. Retrieved from

Ma, T., Lucas, D., Jakirlic, S., & Frohlich, J. (2020). Progress in the second-moment closure for bubbly flow based on direct numerical simulation data. *Journal of Fluid Mechanics, 883*. doi:10.1017/jfm.2019.851

Ma, T., Santarelli, C., Ziegenhein, T., Lucas, D., & Frohlich, J. (2017). Direct numerical simulation-based Reynolds-averaged closure for bubble-induced turbulence. *Physical Review Fluids, 2*(3). doi:10.1103/PhysRevFluids.2.034301

Magolan, B., & Baglietto, E. (2019). Assembling a bubble-induced turbulence model incorporating physical understanding from DNS. *International Journal of Multiphase Flow, 116*, 185-202. doi:10.1016/j.ijmultiphaseflow.2019.04.009

Menter, F. R. (1994). 2-Equation Eddy-Viscosity Turbulence Models for Engineering Applications. *Aiaa Journal, 32*(8), 1598-1605. doi:10.2514/3.12149

Möller, F., Kipping, R., Lavetty, C., Hampel, U., & Schubert, M. (2019). Two-Bubble Class Approach Based on Measured Bubble Size Distribution for Bubble Columns with and without Internals. *Industrial & Engineering Chemistry Research, 58*(8), 2759-2769. doi:10.1021/acs.iecr.8b05784

Morrall, A., Quayle, S., & Campobasso, M. S. (2020). Turbulence modelling for RANS CFD analyses of multi-nozzle annular jet pump swirling flows. *International Journal of Heat and Fluid Flow, 85*. doi:10.1016/j.ijheatfluidflow.2020.108652

Naot, D., & Rodi, W. (1982). Calculation of secondary currents in channel flow. *Journal of the Hydraulics Division-Asce, 108*(8), 948-968.

Neumann-Kipping, M., Bieberle, A., & Hampel, U. (2020). Investigations on bubbly two-phase flow in a constricted vertical pipe. *International Journal of Multiphase Flow, 130*. doi:10.1016/j.ijmultiphaseflow.2020.103340

Neumann, M., Bieberle, M., Wagner, M., Bieberle, A., & Hampel, U. (2019). Improved axial plane distance and velocity determination for ultrafast electron beam x-ray computed tomography. *Measurement Science and Technology, 30*(8). doi:10.1088/1361-6501/ab1ba2

Nicoud, F., & Ducros, F. (1999). Subgrid-scale stress modelling based on the square of the velocity gradient tensor. *Flow Turbulence and Combustion, 62*(3), 183-200.

Olmos, E., Gentric, C., & Midoux, N. (2003). Numerical description of flow regime transitions in bubble column reactors by a multiple gas phase model. *Chemical Engineering Science, 58*(10), 2113-2121. Retrieved from <Go to ISI>://WOS:000184312400015. doi:10.1016/S0009-2509(03)00013-7

Padial, N. T., VanderHeyden, W. B., Rauenzahn, R. M., & Yarbro, S. L. (2000). Three-dimensional simulation of a three-phase draft-tube bubble column. *Chemical Engineering Science, 55*(16), 3261-3273. Retrieved from <Go to ISI>://WOS:000087248400017. doi:Doi 10.1016/S0009-2509(99)00587-4

Parekh, J., & Rzehak, R. (2018). Euler-Euler multiphase CFD-simulation with full Reynolds stress model and anisotropic bubble-induced turbulence. *International Journal of Multiphase Flow, 99*, 231-245. doi:10.1016/j.ijmultiphaseflow.2017.10.012

Pfleger, D., Gomes, S., Gilbert, N., & Wagner, H. G. (1999). Hydrodynamic simulations of laboratory scale bubble columns fundamental studies of the Eulerian-Eulerian modelling approach. *Chemical Engineering Science, 54*(21), 5091-5099. doi:10.1016/s0009-2509(99)00261-4

Sato, Y., & Sekoguchi, K. (1975). Liquid velocity distribution in two-phase bubbly flow *Int. J. Multiphase flow 2*, 79-95.

Shawkat, M. E., Ching, C. Y., & Shoukri, M. (2008). Bubble and liquid turbulence characteristics of bubbly flow in a large diameter vertical pipe. *International Journal of Multiphase Flow, 34*(8), 767-785. doi:10.1016/j.ijmultiphaseflow.2008.01.007

Shi, S. B., Wang, D. W., Qian, Y. L., Sun, X. D., Liu, Y., & Tentner, A. (2020). Liquid-phase turbulence measurements in air-water two-phase flows using particle image velocimetry. *Progress in Nuclear Energy, 124*. doi:10.1016/j.pnucene.2020.103334

Smagorinsky, J. (1963). General circulation experiments with the primitive equations: I. The basic experiment. *Monthly Weather Review, 91*(3), 99-164. doi:10.1175/1520-0493(1963)091<0099:GCEWTP>2.3.CO;2

Sokolichin, A., Eigenberger, G., Lapin, A., & Lubbert, A. (1997). Dynamic numerical simulation of gas-liquid two-phase flows - Euler/Euler versus Euler/Lagrange. *Chemical Engineering Science, 52*(4), 611-626. Retrieved from <Go to ISI>://WOS:A1997WF68700012. doi:Doi 10.1016/S0009-2509(96)00425-3

Song, J., Kharoua, N., Khezzar, L., & Alshehhi, M. (2018). Rans Modelling of a Swirling Flow Interacting with a Conical Bluff Body. *Proceedings of the Asme Fluids Engineering Division Summer Meeting, 2018, Vol 2*.

Speziale, C. G., Sarkar, S., & Gatski, T. B. (1991). Modeling the pressure strain correlation of turbulence - An invariant dynamic-systems approach. *Journal of Fluid Mechanics, 227*, 245-272. doi:10.1017/s0022112091000101

Tabib, M. V., Roy, S. A., & Joshi, J. B. (2008). CFD simulation of bubble column - An analysis of interphase forces and turbulence models. *Chemical Engineering Journal, 139*(3), 589-614. doi:10.1016/j.cej.2007.09.015

Tas-Koehler, S., Lecrivain, G., Krepper, E., Unger, S., & Hampel, U. (2020). Numerical investigation on the effect of transversal fluid field deformation on heat transfer in a rod bundle with mixing vanes. *Nuclear Engineering and Design, 361*. doi:10.1016/j.nucengdes.2020.110575

Tas-Koehler, S., Liao, Y., & Hampel, U. (2021a). A critical analysis of drag force modelling for disperse gas-liquid flow in a pipe with an obstacle. *Chemical Engineering Science, 246*, 117007. doi:10.1016/j.ces.2021.117007

Tas-Koehler, S., Neumann-Kipping, M., Liao, Y. X., Krepper, E., & Hampel, U. (2021b). CFD simulation of bubbly flow around an obstacle in a vertical pipe with a focus on breakup and coalescence modelling. *International Journal of Multiphase Flow, 135*. doi:10.1016/j.ijmultiphaseflow.2020.103528

Tomiyama, A., Tamai, H., Zun, I., & Hosokawa, S. (2002). Transverse migration of single bubbles in simple shear flows. *Chemical Engineering Science, 57*(11), 1849-1858. doi:10.1016/S0009-2509(02)00085-4

Vaidheeswaran, A., & Hibiki, T. (2017). Bubble-induced turbulence modeling for vertical bubbly flows. *International Journal of Heat and Mass Transfer, 115*, 741-752. doi:10.1016/j.ijheatmasstransfer.2017.08.075

Yakhot, V., Orszag, S. A., Thangam, S., Gatski, T. B., & Speziale, C. G. (1992). Development of Turbulence Models for Shear Flows by a Double Expansion Technique. *Physics of Fluids a-Fluid Dynamics, 4*(7), 1510-1520. doi:10.1063/1.858424

Yang, Z. Y. (2015). Large-eddy simulation: Past, present and the future. *Chinese Journal of Aeronautics, 28*(1), 11-24. doi:10.1016/j.cja.2014.12.007

Yeoh, G. H., & Tu, J. Y. (2019). *Computational Techniques for Multiphase Flows*: Elsevier Science & Technology.

Zhang, D., Deen, N. G., & Kuipers, J. A. M. (2006). Numerical simulation of the dynamic flow behavior in a bubble column: A study of closures for turbulence and interface forces. *Chemical Engineering Science, 61*(23), 7593-7608. doi:10.1016/j.ces.2006.08.053